LBNL-42105

ERNEST ORLANDO LAWRENCE
BERKELEY NATIONAL LABORATORY

CONF-971111--

New 3D Parallel GILD Electromagnetic Modeling and Nonlinear Inversion using Global Magnetic Integral and Local Differential Equation

Ganquan Xie, Jianhua Li, Ernest Majer, and D. Zuo

Earth Sciences Division

July 1998

Presented at the
SEG International Exposition
and 67th Annual Meeting,
Dallas, Texas,
November 2–7, 1997,
and the expanded abstract
was published in
the Proceedings

LBNL-42105

NEW 3D PARALLEL GILD ELECTROMAGNETIC MODELING AND NONLINEAR INVERSION USING GLOBAL MAGNETIC INTEGRAL AND LOCAL DIFFERENTIAL EQUATION

Ganquan Xie, Jianhua Li, Ernest Majer, And D. Zuo

Earth Sciences Division

Lawrence Berkeley National Laboratory

July, 1998

This work was supported by the Office of Energy Research, Office of Basic Energy Sciences DOE under Contract No. DE-AC03-76SF00098 partly.

New 3D Parallel GILD Electromagnetic Modeling And Inversion Using The Magnetic Global Integral And Local Differential Equation

Ganquan Xie, Jianhua Li, Ernest L. Majer, and Daxin Zuo

Earth Sciences Division, Bldg. 90, Lawrence Berkeley National Laboratory
1 Cyclotron Road, Berkeley, CA 94720, USA

(July 18, 1998)

ABSTRACT

This paper describes a new 3D parallel GILD electromagnetic (EM) modeling and nonlinear inversion algorithm. The algorithm consists of: (a) a new magnetic integral equation instead of the electric integral equation to solve the electromagnetic forward modeling and inverse problem; (b) a collocation finite element method for solving the magnetic integral and a Galerkin finite element method for the magnetic differential equations; (c) a nonlinear regularizing optimization method to make the inversion stable and of high resolution; and (d) a new parallel 3D modeling and inversion using a global integral and local differential domain decomposition technique (GILD). The new 3D nonlinear electromagnetic inversion has been tested with synthetic data and field data. We obtained very good imaging for the synthetic data and reasonable subsurface EM imaging for the field data. The parallel algorithm has high parallel efficiency over 90% and can be a parallel solver for elliptic, parabolic, and hyperbolic modeling and inversion. The parallel GILD algorithm can be extended to develop a high resolution and large scale seismic and hydrology modeling and inversion in the massively parallel computer.

INTRODUCTION

Three dimensional electromagnetic inversion imaging is an important tool in geophysical exploration, oil reservoir management, and environmental site characterization, because electrical conductivity is directly related to the pore fluid composition, porosity, and saturation of the rocks. Ill-posedness, strong nonlinearity and high computational costs are the main difficulties in developing 3D nonlinear electromagnetic inversion algorithms and software. Nevertheless active work continues in this area. Habashy, Groom, and Spies (1993) developed the static localized nonlinear approximation and localized nonlinear extended Born approximation. Zhou et al. (1993) developed an audio-frequency electromagnetic tomography in 2D. Habashy, Oristaglo, and de Hoop (1994) developed a simultaneous nonlinear reconstruction of two dimensional permittivity and conductivity. Lee and Xie (1993) developed an electromagnetic crosshole imaging. Nekut (1994) developed an electromagnetic raytrace tomography. Mackie and Maden (1993) developed a 3D MT inversion scheme using conjugate gradients. Pellerin et al. (1993) developed a three-dimensional inversion of electromagnetic data. Chen and Kim (1995) developed a parallel algorithm for inverse scattering problems of Maxwell's equations on hypercubes. Ellis (1995) developed a joint 3D electromagnetic inversion. Li et al. (1995) developed a nonlinear three-dimensional inverse imaging for direct current data. Torres-Verdin and Habashy investigated the 2D electromagnetic inverse problem by the extended Born approximation. Newman (1995) developed crosswell electromagnetic inversion using integral and differential equations. Newman and Alumbaugh (1995) developed 3D massively parallel electromagnetic inversion. Zhdanov and Fang (1995) developed a 3D quasi-linear electromagnetic inversion. In the past 3 years, we have developed two kinds of 3D nonlinear electromagnetic inversion schemes, one using the magnetic field integral equation and the other using the electric field integral equation (Xie et al., 1995a, 1995b). In this paper, we developed an algorithm that consists of: (a) a new magnetic integral equation instead of the electric integral equation to solve the electromagnetic forward modeling and inverse problem; (b) a collocation finite element method for solving the magnetic integral and a Galerkin finite element method for the magnetic differential equations; (c) a nonlinear regularizing optimization method to make the inversion stable and of high resolution; (d) a new parallel 3D inversion algorithm using a global integral and local differential (GILD) domain decomposition technique. The main advantages of the new magnetic integral equation and GILD algorithm are: (a) the magnetic field in the magnetic integral equation remains continuous when electric conductivity is discontinuous, which is convenient for using the finite element method; (b) the kernel function in the magnetic integral equation exhibits as integrative weakly singularity; (c) there is a natural relative difference term in the magnetic integral equation; (d) there is no artificial boundary condition needed in the GILD modeling and inversion; and (e) the computational time and storage are reduced. The plan of this paper is as follows. The introduction has been already presented in this section. In the next section, we derive the new 3D magnetic integral equation for the magnetic field, new electric integral equation for the electric field, and their corresponding differential equations for forward modeling. The 3D nonlinear EM inversion using the new magnetic integral equation globally and differential equations locally will be presented in the section "3D EM inversion using integral and differential equations". In the next section, we describe a finite element method for solution of the magnetic integral and differential equations on the modeling and inversion. The nonlinear regularizing optimization methods and their optimum regularizing parameters will be presented in section "regularizing method". In the next section, we describe a parallel GILD algorithm for the forward and inverse problems by using a global integral and local differential domain decomposition technique. For completeness, we used the section "electric field calculation" to describe the finite element approximation of the electric field. Many applications are presented in section "applications". Finally, we describe some conclusions.

NEW 3D ELECTROMAGNETIC INTEGRAL EQUATIONS

New magnetic integral equation

From the Maxwell equations,

$$\nabla \times E = -i\omega\mu(H + M_s) \tag{1}$$

and

$$\nabla \times H = (\sigma + i\omega\varepsilon)E + J_c, \tag{2}$$

the electric integral equation can be derived (Raiche 1974, Hohmann 1975, Weidelt 1975, Habashy et al., 1993, Torres-Verdin and Habashy 1994),

$$E\left(r\right) = E_b\left(r\right) - i\omega\mu \int\limits_{V_s} G_b^E\left(r, r'\right)\left[\left(\sigma - \sigma_b\right) + i\omega\left(\varepsilon - \varepsilon_b\right)\right] E\left(r'\right) dr'. \tag{3}$$

Where E is the total electric field, E_b is the background layered earth electric field, H is the total magnetic field, μ is the magnetic permeability, σ is the electric conductivity, ε is the permittivity, ω is the angular frequency, σ_b and ε are the layered background electric conductivity and permittivity, J_c is the electric current source term, M_s is the magnetic moment source term, and points r and r' are in V_s, V_s is the finite bounded scattering volume domain in which $\sigma - \sigma_b + i\omega(\varepsilon - \varepsilon_b) \neq 0$. In this paper, the background layered parameters, σ_b and ε_b are known. $G_b^E\left(r, r'\right)$ is the layered background electric Green's function,

$$G_b^E\left(r, r'\right) = \left(I + \frac{1}{k_b^2}\nabla_{r'}\nabla_{r'}\right) g_b\left(r, r'\right) + G_s^E\left(r, r'\right), \tag{4}$$

where

$$g_b\left(r, r'\right) = \frac{e^{-ik_b|r-r'|}}{4\pi\left|r - r'\right|}, \tag{5}$$

$$k_b^2 = -i\omega\mu\left(\sigma_b + i\omega\varepsilon_b\right), \tag{6}$$

$$|r - r'| = \sqrt{(x-x')^2 + (y-y')^2 + (z-z')^2}. \tag{7}$$

In the equations above, $G_s^E(r, r')$ is the layer contribution apart from the whole space part of the Green's function, $g_b(r, r')$ is the whole space Green's function, and I is the 3×3 identity matrix. Taking the curl of both sides of equation (3), using $\nabla_r \times G_b^E(r, r') = \nabla_r \times (g_b(r, r') I) + \nabla_r \times G_s^E(r, r')$ and $\nabla_r \times (g_b(r, r') I) = -\nabla_{r'} g_b(r, r') \times I$, changing the curl operator from the unprime to the prime coordinate, using the formula (2), and manipulating some calculations, we obtain the following new magnetic integral equation (Xie et al. 1995a)

$$\begin{aligned} H(r) = H_b(r) - \int_{V_s} \nabla_{r'} g_b(r, r') \times \tfrac{(\sigma-\sigma_b)+i\omega(\varepsilon-\varepsilon_b)}{\sigma+i\omega\varepsilon} (\nabla_{r'} \times H - J_c)\, dr' \\ + \int_{V_s} \nabla_r \times G_s^E(r, r') \tfrac{(\sigma-\sigma_b)+i\omega(\varepsilon-\varepsilon_b)}{\sigma+i\omega\varepsilon} (\nabla_{r'} \times H - J_c)\, dr', \end{aligned} \tag{8}$$

where H is the magnetic field to be found, H_b is the background magnetic field, ∇_r is the grad over the variable r, and $\nabla_{r'}$ is the grad over the variable r'. Even though the magnetic integral equation (8) is equivalent to the electric integral equation (3) theoretically, they are not equivalent numerically. The magnetic field in (8) is continuous when the electric conductivity is discontinuous, but the electric field in (3) is discontinuous when the electric conductivity is discontinuous. In the integral equation (8), the unknown function is only the magnetic field H, but not the discontinuous term $\nabla \times H$. When the magnetic permeability is continuous, the electric conductivity and permittivity are discontinuous but piecewise continuous, (i.e., let $V_{dis} \subset V_s$ be a point set where σ and ε vary discontinuously, the volume of the set V_{dis} is zero, $\int_{V_{dis}} dr = 0$.), then the magnetic field H has the following properties: (a) It is continuous and piecewise differentiable; (b) $\nabla \times H$ is bounded and piecewise continuous; (c) The discontinuity of $\nabla \times H$ does not influence on the magnetic integral equation (8) because the volume integral of $\nabla \times H$ on the discontinuous set V_{dis} is zero, $\int_{V_{dis}} \nabla \times H dr = 0$; (d) The magnetic field H satisfies the following integral inequality,

$$\omega\mu \int_{V_s} |H(r)|^2 dr + \int_{V_s} \frac{1}{|\sigma + i\omega\varepsilon|} |\nabla \times H|^2 \, dr < B(H) < \infty, \tag{9}$$

where $B(H)$ is a finite number that is depended on the magnetic field H; The physical meaning of the above inequality (9) is that the energy of the magnetic field is finite; (e) The singular part, $\nabla_{r'} g_b(r, r')$, of the kernel function in (8) is the integrative weakly singular term, $\int\limits_{V_{dis}} \nabla_r g\,(r, r') dr' = 0$, and $\int\limits_{V_{dis}} \nabla_r g\,(r, r') \times (\nabla \times H)\, dr' = 0$, but the kernel function in (3) involves the strongly singular term $\frac{1}{k_b^2} \nabla_{r'} \nabla_{r'} g_b(r, r')$. These properties of the magnetic integral equation (8) are important for using finite element method and guarantee the convergence of its finite element approximation.

Magnetic differential equation

Suppose that $\sigma + i\omega\varepsilon \neq 0$, dividing $\sigma + i\omega\varepsilon$ and taking the curl of both sides of equation (2), and using equation (1), we have a magnetic differential equation

$$\nabla \times \left(\frac{1}{\sigma + i\omega\varepsilon} \nabla \times H \right) + i\omega\mu H = P_s, \tag{10}$$

where source term P_s is as follows,

$$P_s = \nabla \times \frac{J_c}{\sigma + i\omega\varepsilon} - i\omega\mu M_s.$$

The above magnetic integral equation (8) and the magnetic differential equation (10) are convenient to use the finite element method for magnetic field in an isotropic heterogeneous electric conductivity σ and permittivity ε and constant magnetic permeability μ medium. The magnetic integral equation (8) on the boundary and the magnetic differential equation (10) in the internal domain is coupled to construct a new GILD magnetic-electric modeling that will be described later.

New electric integral equation

In an isotropic heterogeneous magnetic permeability μ and constant electric conductivity σ and permittivity ε medium, a new electric integral equation by Li and Xie (1997) and Xie et. al (1995) can be written following as

$$\begin{aligned} E\left(r\right) = E_b\left(r\right) - \int_{V_s} \nabla_{r'} g_b(r,r') \times \tfrac{\mu-\mu_b}{\mu}\left(\nabla_{r'} \times E - M_s\right) dr' \\ + \int_{V_s} \nabla_r \times G_s^H\left(r,r'\right) \tfrac{\mu-\mu_b}{\mu}\left(\nabla_{r'} \times E - M_s\right) dr', \end{aligned} \qquad (11)$$

and its corresponding the electric differential equation follows, as

$$\nabla \times \left(\frac{1}{\mu}\nabla \times E\right) + i\omega\left(\sigma + i\omega\varepsilon\right)E = Q_s, \qquad (12)$$

where the source term

$$Q_s = -i\omega\left(J_c + \nabla \times M_s\right), \qquad (13)$$

are suitable for determining the electric field. The electric integral equation (11) on the boundary and the electric differential equation (12) in the internal domain is coupled to construct a new GILD electric-magnetic modeling. In the equations above, μ is the magnetic permeability to be defined, μ_b is the background magnetic permeability, $G_s^H\left(r,r'\right)$ is the background secondary magnetic Green's function, M_s is a magnetic source term, J_c is a electric source term, E_b is the background electric field, V_s is the scattering integral domain in which $\mu - \mu_b \neq 0$, and σ, ε are constants.

3D NONLINEAR EM INVERSION USING INTEGRAL AND DIFFERENTIAL EQUATIONS

The following nonlinear magnetic integral equation can be used to find σ and ε from the measured magnetic field data H_d:

$$\begin{aligned} H_d\left(r\right) = H_b\left(r\right) - \int_{V_s} \nabla_{r'} g_b(r,r') \times \tfrac{(\sigma-\sigma_b)+i\omega(\varepsilon-\varepsilon_b)}{\sigma+i\omega\varepsilon}\left(\nabla_{r'} \times H - J_c\right) dr' \\ + \int_{V_s} \nabla_r \times G_s^E\left(r,r'\right) \tfrac{(\sigma-\sigma_b)+i\omega(\varepsilon-\varepsilon_b)}{\sigma+i\omega\varepsilon}\left(\nabla_{r'} \times H - J_c\right) dr'. \end{aligned} \qquad (14)$$

The integral equation (14) is similar to (8) in form, but they are used differently. The equation (8) is a linear Fredholm integral equation of the second kind for magnetic field $H(r)$ with $r \in V_s$. The equation (14) is a nonlinear Fredholm integral equation of the first kind for the electric conductivity $\sigma(r)$ and permittivity $\varepsilon(r)$ with r at the receiver site. In the integral equation (14), the magnetic field H is the solution of the integral equation (8) and is also a nonlinear operator of σ and ε. Because equation (14) is essentially ill-posed and underdetermined when there are not enough data, we translate (14) to the following nonlinear optimization problem instead of solving it directly.

$$\begin{aligned}\sum_{\ell=1}^{n_r}\sum_{l=1}^{n_{fs}}\Bigg\| & H_{d,l}\left(r_\ell\right) - H_{b,l}\left(r_\ell\right) + \int_{V_s} \nabla_{r'} g_b(r_\ell, r') \times \frac{(\sigma-\sigma_b)+i\omega(\varepsilon-\varepsilon_b)}{\sigma+i\omega\varepsilon}\left(\nabla_{r'} \times H_l - J_{c_l}\right) dr' \\ & - \int_{V_s} \nabla_r \times G_s^E\left(r_\ell, r'\right) \frac{(\sigma-\sigma_b)+i\omega(\varepsilon-\varepsilon_b)}{\sigma+i\omega\varepsilon}\left(\nabla_{r'} \times H_l - J_{c_l}\right) dr' \Bigg\|^2 = \min, \end{aligned} \qquad (15)$$

where $\ell = 1, \cdots, n_r$, n_r is the number of receivers, $l = 1, \cdots, n_{fs}$, $n_{fs} = n_f \times n_s$, n_f is the number of frequencies, n_s is the number of sources. From the magnetic integral equation (14), we known that the magnetic field H is a nonlinear operator depended on the electric conductivity and permittivity. Let $\Im$ be the Jacobian operator of (14), then $\Im$ satisfies

$$\Im\delta(\sigma + i\omega\varepsilon) = \delta H, \qquad (16)$$

where δH is the variation of the nonlinear operator H. We approximate the variation δH by δH_1 and δH_2, where δH_1 is the first order term

$$\begin{aligned}\delta H_1\left(r\right) = & \int_{V_s} \nabla_{r'} g_b(r, r') \times \frac{\delta(\sigma+i\omega\varepsilon)}{\sigma+i\omega\varepsilon}\frac{(\sigma_b+i\omega\varepsilon_b)}{\sigma+i\omega\varepsilon}\left(\nabla_{r'} \times H - J_c\right) dr' \\ & - \int_{V_s} \nabla_r \times G_s^E\left(r, r'\right) \frac{\delta(\sigma+i\omega\varepsilon)}{\sigma+i\omega\varepsilon}\frac{(\sigma_b+i\omega\varepsilon_b)}{\sigma+i\omega\varepsilon}\left(\nabla_{r'} \times H - J_c\right) dr', \end{aligned} \qquad (17)$$

and

$$\begin{aligned}\delta H_2\left(r\right) = & \int_{V_s} \nabla_{r'} g_b(r, r') \times \frac{\delta(\sigma+i\omega\varepsilon)}{\sigma+i\omega\varepsilon}\frac{(\sigma_b+i\omega\varepsilon_b)}{\sigma+i\omega\varepsilon}\left(\nabla_{r'} \times H - J_c\right) dr' \\ & - \int_{V_s} \nabla_r \times G_s^E\left(r, r'\right) \frac{\delta(\sigma+i\omega\varepsilon)}{\sigma+i\omega\varepsilon}\frac{(\sigma_b+i\omega\varepsilon_b)}{\sigma+i\omega\varepsilon}\left(\nabla_{r'} \times H - J_c\right) dr' \\ & - \int_{V_s} \nabla_{r'} g_b(r, r') \times \frac{(\sigma-\sigma_b)+i\omega(\varepsilon-\varepsilon_b)}{\sigma+i\omega\varepsilon}\nabla_{r'} \times \delta H_1 \; dr' \\ & + \int_{V_s} \nabla_r \times G_s^E\left(r, r'\right) \frac{(\sigma-\sigma_b)+i\omega(\varepsilon-\varepsilon_b)}{\sigma+i\omega\varepsilon}\nabla_{r'} \times \delta H_1 \; dr', \end{aligned} \qquad (18)$$

is a higher order approximation that accounts for some of the nonlinearly in equation (16).

As described later, δH_1, δH_2 and the Jacobian operator $\Im$ are used in the Gauss-Newton iteration for solving the nonlinear optimization problem in equation (15). The full matrix required for the Gauss-Newton iteration needs large storage and significant computational time costs are involved. To overcome this difficulty, a new global integral and local differential decomposition algorithm has been developed (Xie and Li, 1997a and 1997b). For the electric conductivity and permittivity inversion algorithm, we employ the nonlinear magnetic integral optimization (equation (15)) with the following magnetic variation differential equation,

$$\nabla \times \left(\frac{\delta\sigma + i\omega\delta\varepsilon}{(\sigma + i\omega\varepsilon)^2} \nabla \times H \right) = \nabla \times \left(\frac{1}{\sigma + i\omega\varepsilon} \nabla \times \delta H \right) + i\omega\mu\delta H, \tag{19}$$

to assemble a global integral and local differential decomposition; equation (19) is obtained by perturbing equation (9) in the σ and ε. Similary, in the magnetic permeability inversion, the following nonlinear electric integral optimization problem can be formulated, where

$$\sum_{\ell=1}^{n_r} \sum_{l=1}^{n_{fs}} \Bigg\| E_{d,l}(r_\ell) - E_{b,l}(r_\ell) + \int_{V_s} \nabla_{r'} g_b(r_\ell, r') \times \tfrac{\mu-\mu_b}{\mu} \left(\nabla_{r'} \times E_l - M_{s_l} \right) dr' \\ - \int_{V_s} \nabla_r \times G_s^H(r_\ell, r') \tfrac{\mu-\mu_b}{\mu} \left(\nabla_{r'} \times E_l - M_{s_l} \right) dr \Bigg\|^2 = \min, \tag{20}$$

with the electric variation differential equation,

$$\nabla \times \left(\frac{\delta\mu}{\mu^2} \nabla \times E \right) = \nabla \times \left(\frac{1}{\mu} \nabla \times \delta E \right) + i\omega(\sigma + i\omega\varepsilon)\delta E, \tag{21}$$

obtained by perturbing equation (12) in the electrical properties. Equations (15) and (19), (20) and (21) are assembled and constructed the GILD decomposition solution. In this paper, however, we confine ourselves to the electric conductivity and permittivity inversion. The magnetic permeability inversion will be presented in a subsequent paper.

DISCRETIZATION OF THE INTEGRAL AND DIFFERENTIAL EQUATIONS USING THE FINITE ELEMENT METHOD

Finite element approximations

The domain V_s is divided into a set of finite cubic block elements, V_e, $e = 1, 2, ..., M$, where the M is total member of the elements in the domain V_s, $V_e \bigcap V_{e'} = 0$ if $e \neq e'$, and $V_s = \bigcup_{e=1}^{M} V_e$. We use a linear finite element approximation functions with point collocation to discretize the magnetic integral equations (8) and (15) and the Galerkin finite element method to discretize equations (9) and (19). There are 8 vertex nodes in each element. The magnetic field value H_j is assigned at each node, the electric conductivity value σ_e, the background conductivity value $\sigma_{b,e}$, permittivity value ε_e, and background permittivity value $\varepsilon_{b,e}$ are assigned in each element. Let (x_i, y_i, z_i) be the coordinates of the vertex i, and let l, h, and v be the lengths of the sides of the element in the x, y, and z directions, respectively. The trilinear finite element approximation vector function H^h can be constructed with base functions ϕ_j by Xie (1975).

$$H^h(x,y,z) = \sum_{j=1}^{8} H_j \phi_j(x,y,z), \tag{22}$$

where

$$H^h(x,y,z) = \begin{pmatrix} H_x^h(x,y,z) \\ H_y^h(x,y,z) \\ H_z^h(x,y,z) \end{pmatrix}, \tag{23}$$

and

$$H_j = \begin{pmatrix} H_{xj} \\ H_{yj} \\ H_{zj} \end{pmatrix}. \tag{24}$$

In each cubic element, the base magnetic field is a trilinear function,

$$\phi_j(x,y,z) = \frac{(x - x_j^*)(y - y_j^*)(z - z_j^*)}{(l - 2x_j^*)(h - 2y_j^*)(v - 2z_j^*)}, \tag{25}$$

where

$$(x_1^*, x_2^*, x_3^*) = (l, h, v)\,, \cdots, (x_8^*, x_8^*, x_8^*) = (0, 0, 0)\,, \tag{26}$$

and

$$(x_1, y_1, z_1) = (0, 0, 0), \cdots, (x_8, y_8, z_8) = (l, h, v). \tag{27}$$

Finite element magnetic integral equation for modeling

Upon substituting (22)-(25) and their derivatives into (8), we have

$$\begin{aligned} H^h(r) = H_b^h(r) - \int_{V_s} \nabla_{r'} g_b(r, r') \times \tfrac{(\sigma-\sigma_b)+i\omega(\varepsilon-\varepsilon_b)}{\sigma+i\omega\varepsilon} \left(\nabla_{r'} \times H^h - J_c\right) dr' \\ + \int_{V_s} \nabla_r \times G_s^E(r, r') \tfrac{(\sigma-\sigma_b)+i\omega(\varepsilon-\varepsilon_b)}{\sigma+i\omega\varepsilon} \left(\nabla_{r'} \times H^h - J_c\right) dr', \end{aligned} \tag{28}$$

Because (a) H^h is continuous and piecewise differentiable; (b) $\nabla \times H$ is bounded and piecewise continuous and the linear function in each element V_e; (c) the discontinuous set V_{dis} of $\nabla \times H$ is the set of the inter boundary between the elements; (d) the discontinuity of $\nabla \times H^h$ does not influence on the magnetic integral equation (28) because the volume integral of $\nabla \times H^h$ on the discontinuous set V_{dis} is zero, $\int_{V_{dis}} \nabla \times H^h dr = 0$, and $\int_{V_{dis}} \left(\nabla_{r'} g(r, r') - \nabla_r \times G_s^E(r, r')\right) \times (\nabla \times H)\, dr' = 0$; (e) the magnetic field H^h satisfies the integral inequality (9) and belong to the Sobolev space $\Re$ (Ciarlet 1978, Xie 1981, and Xie and Chen (1985)). We can present the integral of (28) in the V_s as the summation of the integral in the cubic elements,

$$\begin{aligned} H^h(r) = H^h{}_b(r) - \sum_{e=1}^{M} \tfrac{(\sigma_e-\sigma_b)+i\omega(\varepsilon_e-\varepsilon_b)}{\sigma_e+i\omega\varepsilon_e} \int_{V_e} \nabla_{r'} g_b(r, r') \times \left(\nabla_{r'} \times H^h(r') - J_c\right) dr' \\ + \sum_{e=1}^{M} \tfrac{(\sigma_e-\sigma_b)+i\omega(\varepsilon_e-\varepsilon_b)}{\sigma_e+i\omega\varepsilon_e} \int_{V_e} \nabla_r \times G_b^E(r, r') \cdot \left(\nabla_{r'} \times H^h(r') - J_c\right) dr'. \end{aligned} \tag{29}$$

Upon substituting the expressions of H^h, (23)-(25), into the (29) and giving the node location coordinate, r_i, the integral in each element V_e of the discrete integral equation (29)

$$
\begin{aligned}
&\int_{V_e} \nabla_{r'} g_b(r_i, r') \times \tfrac{(\sigma-\sigma_b)+i\omega(\varepsilon-\varepsilon_b)}{\sigma+i\omega\varepsilon} \left(\nabla_{r'} \times H^h\right) dr' \\
&-\int_{V_e} \nabla_r \times G_s^E\left(r_i, r'\right) \tfrac{(\sigma-\sigma_b)+i\omega(\varepsilon-\varepsilon_b)}{\sigma+i\omega\varepsilon} \left(\nabla_{r'} \times H^h\right) dr' \\
&\qquad = \sum_{j=1}^{8} K_{i,j}^e {H^h}_j,
\end{aligned}
\tag{30}
$$

where

$$
\begin{aligned}
K_{i,j}^e = {} & \tfrac{\left(\sigma_e-\sigma_{b,e}\right)+i\omega\left(\varepsilon_e-\varepsilon_{b,e}\right)}{\sigma_e+i\omega\varepsilon_e} \int_{V_e} \nabla_{r'} g_b(r_i, r') \times \left(\nabla_{r'} \times \phi_j\right) dr' \\
& - \tfrac{\left(\sigma_e-\sigma_{b,e}\right)+i\omega\left(\varepsilon_e-\varepsilon_{b,e}\right)}{\sigma_e+i\omega\varepsilon_e} \int_{V_e} \nabla_r \times G_s^E\left(r_i, r'\right) \left(\nabla_{r'} \times \phi_j\right) dr', \\
& i = 1, 2, \cdots, N, j = 1, 2, \cdots, 8,
\end{aligned}
\tag{31}
$$

The integral in (31) is evaluated using the Gaussian numerical integral formulation. When the length of the mesh is going to zero, the equation (28) is approximation to the equation (8). The solution of (28), $H^h(r)$, is a finite element approximation of the solution of the magnetic integral equation (8). After calculating and arrangements, we obtain the total matrix equation for the discrete magnetic field:

$$
(I + K)H^h = S,
\tag{32}
$$

where

$$
K = \begin{bmatrix} K_1 \\ K_2 \\ \vdots \\ K_i \\ \vdots \\ K_N \end{bmatrix}.
\tag{33}
$$

This matrix K is a full matrix and

$$
K_i = \sum_{e=1}^{M} \sum_{j=1}^{8} K_{i,j}^e,
\tag{34}
$$

where N is the number of total nodes, $H^h = (H_1, H_2, \cdots, H_N)^T$ is an unknown vector of the magnetic field value at nodes, and S is the source vector. The discrete equation (32) is the full matrix equation. The high cost of computation time and storage is a serious limitation of the discrete integral equation (32), but it is needn't any artificial boundary condition that is a great merit of (32). In the section of the "parallel GILD modeling and inversion algorithm", we don't need to solve the complete discrete integral equation. The discrete integral equation only is built on the boundary, i.e, the r_i are only the boundary node of the domain in (30)-(31). The discrete integral equation on the boundary node and discrete differential equation in the internal node will be coupled to construct a GILD modeling.

Finite element magnetic differential equation for modeling

In the paper by Xie et al. (1995c), a finite element scheme for the 3D magnetic differential equation was presented. The Galerkin equation of (10) will be

$$\int_{V_s} \left(\frac{1}{\sigma+i\omega\varepsilon}(\nabla \times H)\cdot(\nabla \times [\phi_i]) + i\omega\mu H \cdot [\phi_i]\right)dv$$
$$= \int_{V} P_s \cdot [\phi_i] dv, \tag{35}$$

where the P_s is the source term, and $[\phi_i]$ is the 3×3 base function matrix , $[\phi_i] = \phi_i[I]$, the I is 3×3 identify matrix and the ϕ_i was described in (25). Substituting (22)-(25) into (35), we obtain the finite element equation of the magnetic Maxwell equation (10)

$$KH^h = S. \tag{36}$$

In the equation above, K, the stiffness matrix is a sparse one, H^h is the discrete magnetic field to be found, S is the discrete source term. K is given by

$$K = \sum_{e=1}^{M} K_{i,j}^e, \tag{37}$$

where

$$K_{i,j}^e = \int_{V_e} \frac{1}{\sigma_e+i\omega\varepsilon_e} \begin{pmatrix} \frac{\partial\phi_i}{\partial y}\frac{\partial\phi_j}{\partial y} + \frac{\partial\phi_i}{\partial z}\frac{\partial\phi_j}{\partial z} & -\frac{\partial\phi_i}{\partial y}\frac{\partial\phi_j}{\partial x} & -\frac{\partial\phi_i}{\partial z}\frac{\partial\phi_j}{\partial x} \\ -\frac{\partial\phi_i}{\partial x}\frac{\partial\phi_j}{\partial y} & \frac{\partial\phi_i}{\partial x}\frac{\partial\phi_j}{\partial x} + \frac{\partial\phi_i}{\partial z}\frac{\partial\phi_j}{\partial z} & -\frac{\partial\phi_i}{\partial z}\frac{\partial\phi_j}{\partial y} \\ -\frac{\partial\phi_i}{\partial x}\frac{\partial\phi_j}{\partial z} & -\frac{\partial\phi_i}{\partial y}\frac{\partial\phi_j}{\partial z} & \frac{\partial\phi_i}{\partial x}\frac{\partial\phi_j}{\partial x} + \frac{\partial\phi_i}{\partial y}\frac{\partial\phi_j}{\partial y} \end{pmatrix} dv$$

$$+ i\omega\mu \int\limits_{V_e} \begin{pmatrix} \phi_i\phi_j & 0 & 0 \\ 0 & \phi_i\phi_j & 0 \\ 0 & 0 & \phi_i\phi_j \end{pmatrix} dv,$$

$$i, j = 1, \cdots, 8. \tag{38}$$

In the forward modeling, K and S in (36) are known, and the discrete magnetic field H^h will be found by solving (36). The finite element discrete magnetic integral equations (31)-(34) is built on the boundary and the finite element discrete magnetic differential equation (36)-(38) is built in the domain that will be assembled to construct a global integral and local differential parallel modeling. A parallel multi-level algorithm will be used to solve the equation from domain to the boundary that will be described in a later section.

Finite element approximation of normal equations for inversion

Let H_{data} be the field measured data with noise, H_{model} be the numerical realization of data, and H^h be the finite element discrete magnetic field.

Define

$$\|H_{data} - H_{model}\|^2 =$$

$$\sum_{\ell=1}^{n_r} \sum_{l=1}^{n_{fs}} \left\| H_{d,l}(r_\ell) - H_{b,l}(r_\ell) + \int\limits_{V_s} \nabla_{r'} g_b(r_\ell, r') \times \tfrac{(\sigma-\sigma_b)+i\omega(\varepsilon-\varepsilon_b)}{\sigma+i\omega\varepsilon} \left(\nabla_{r'} \times H_l{}^h - J_{c_l}\right) dr' \right.$$

$$\left. - \int\limits_{V_s} \nabla_r \times G_s^E(r_\ell, r') \tfrac{(\sigma-\sigma_b)+i\omega(\varepsilon-\varepsilon_b)}{\sigma+i\omega\varepsilon} \left(\nabla_{r'} \times H_l{}^h - J_{c_l}\right) dr' \right\|^2 . \tag{39}$$

The discrete nonlinear optimization problem in equation (15) will be

$$\|H_{data} - H_{model}\|^2 = \min . \tag{40}$$

The Gauss-Newton iterative method is used to solve the nonlinear optimization (40). The normal equations are as follows,

$$\left[\Im^{h\,T}_{\ell,l} \Im^{h}{}_{\ell,l} \right] \delta(\sigma + i\omega\varepsilon) = -\Im^{h\,T}_{\ell,l} \left[H_{d,l}(r_\ell) - H_{b,l}(r_\ell) \right.$$

$$
\begin{aligned}
&+\int\limits_{V_s} \nabla_{r'} g(r_\ell, r') \times \tfrac{(\sigma-\sigma_b)+i\omega(\varepsilon-\varepsilon_b)}{\sigma+i\omega\varepsilon} \left(\nabla_{r'} \times {H_l}^h - J_{c_l}\right) dr' \\
&\left.-\int\limits_{V_s} \nabla_r \times G_s^E(r_\ell, r') \tfrac{(\sigma-\sigma_b)+i\omega(\varepsilon-\varepsilon_b)}{\sigma+i\omega\varepsilon} \left(\nabla_{r'} \times {H_l}^h - J_{c_l}\right) dr' \right], \qquad (41)
\end{aligned}
$$

where $\Im_{\ell,l}^h$ is the finite element discrete representation of the Jacobian operators $\Im_{\ell,l}$ given by equation (16). Depending on the accuracy desired, either one of the approximate Jacobian operations, $\Im^h_{1,\ell,l}$ and $\Im^h_{2,\ell,l}$, are employed, where

$$
\begin{aligned}
\Im^h_{1,\ell,l}(r_\ell) = &\sum_{e=1}^{M} \int\limits_{V_e} \nabla_{r'} g_b(r_\ell, r') \times \left(\nabla_{r'} \times {H_l}^h - J_{c_l}\right) \tfrac{\sigma_{b,e}+i\omega\varepsilon_{b,e}}{\sigma_e+i\omega\varepsilon_e} \tfrac{\psi_e}{\sigma_e+i\omega\varepsilon_e} dr' \\
&-\sum_{e=1}^{M} \int\limits_{V_e} \nabla_r \times G_s^E(r_\ell, r') \left(\nabla_{r'} \times {H_l}^h - J_{c_l}\right) \tfrac{\sigma_{b,e}+i\omega\varepsilon_{b,e}}{\sigma_e+i\omega\varepsilon_e} \tfrac{\psi_e}{\sigma_e+i\omega\varepsilon_e} dr', \qquad (42)
\end{aligned}
$$

and

$$
\begin{aligned}
\Im^h_{2,\ell,l}(r_\ell) = &\sum_{e=1}^{M} \int\limits_{V_e} \nabla_{r'} g_b(r_\ell, r') \times \left(\nabla_{r'} \times {H_l}^h - J_{c_l}\right) \tfrac{\sigma_{b,e}+i\omega\varepsilon_{b,e}}{\sigma_e+i\omega\varepsilon_e} \tfrac{\psi_e}{\sigma_e+i\omega\varepsilon_e} dr' \\
&-\sum_{e=1}^{M} \int\limits_{V_e} \nabla_r \times G_s^E(r_\ell, r') \left(\nabla_{r'} \times {H_l}^h - J_{c_l}\right) \tfrac{\sigma_{b,e}+i\omega\varepsilon_{b,e}}{\sigma_e+i\omega\varepsilon_e} \tfrac{\psi_e}{\sigma_e+i\omega\varepsilon_e} dr' \\
&+\sum_{e'=1}^{M} \int\limits_{V_{e'}} \nabla_{r''} \times Q_1(r_\ell, r'') \cdot \left(\nabla_{r''} \times {H_l}^h - J_{c_l}\right) \tfrac{\sigma_{b,e'}+i\omega\varepsilon_{b,e'}}{\sigma_{e'}+i\omega\varepsilon_{e'}} \tfrac{\psi_{e'}}{\sigma_{e'}+i\omega\varepsilon_{e'}} dr'' \\
&+\sum_{e'=1}^{M} \int\limits_{V_{e'}} Q_2(r_\ell, r'') \cdot \left(\nabla_{r''} \times {H_l}^h - J_{c_l}\right) \tfrac{\sigma_{b,e'}+i\omega\varepsilon_{b,e'}}{\sigma_{e'}+i\omega\varepsilon_{e'}} \tfrac{\psi_{e'}}{\sigma_{e'}+i\omega\varepsilon_{e'}} dr'', \qquad (43)
\end{aligned}
$$

where $\psi_e(r) = 1$, if r in element e, otherwise $\psi_e(r) = 0$, the 3×3 matrices Q_1 and Q_2 are

$$
\begin{aligned}
&Q_1(r, r'') = \sum_{e=1}^{M} \int\limits_{V_e} \tfrac{(\sigma_e-\sigma_{b,e})+i\omega(\varepsilon_e-\varepsilon_{b,e})}{\sigma_e+i\omega\varepsilon_e} \\
&\left\{\left(\nabla_{r'} g_b(r, r') \times I - \nabla_r \times G_s^E(r, r')\right) \left(\nabla_{r'} g_b(r', r'') \times I\right)\right\} dr', \qquad (44)
\end{aligned}
$$

and

$$
\begin{aligned}
&Q_2(r, r'') = \sum_{e=1}^{M} \int\limits_{V_e} \tfrac{(\sigma_e-\sigma_{b,e})+i\omega(\varepsilon_e-\varepsilon_{b,e})}{\sigma_e+i\omega\varepsilon_e} \\
&\left\{\left(\nabla_{r'} g_b(r, r') \times I - \nabla_r \times G_s^E(r, r')\right) \left(\nabla_{r'} \times \nabla_{r'} \times G_s^E(r', r'')\right)\right\} dr'. \qquad (45)
\end{aligned}
$$

Finite element magnetic differential variation equation for inversion

In the electric conductivity and permittivity inversion, we used the Galerkin finite element method to discretize the magnetic variation differential equation (19). The Galerkin equation of (19) is

$$\begin{aligned}&\int\limits_{V_s} \left(\tfrac{\delta(\sigma+i\omega\varepsilon)}{(\sigma+i\omega\varepsilon)^2} (\nabla \times H) \cdot (\nabla \times [\phi_i])\right) dv \\ &= \int\limits_{V_s} \left(\tfrac{1}{\sigma+i\omega\varepsilon} (\nabla \times \delta H) \cdot (\nabla \times [\phi_i]) + i\omega\mu\delta H \cdot [\phi_i]\right) dv.\end{aligned} \tag{46}$$

Upon substituting (22)-(25) and their derivatives into (46), we obtain the finite element equation of (19), make a perturbation of which expression, where

$$H^{h^T}\Gamma\left(\delta\sigma + i\omega\delta\varepsilon\right) = \delta H^{h^T} K. \tag{47}$$

In the equation above, Γ is a sparse matrix, K is a sparse stiffness matrix in (36), $\delta H^h = H^{h^{(n)}} - H^{h^{(n-1)}}$ is a local approximate variation, $H^{h^{(n)}}$ is a finite element magnetic field at n'th iteration, $(\ .\ )^T$ denotes the transport of a vector. Γ is given by

$$\Gamma = \sum_{e=1}^{M} \Gamma_{i,j}^{e}, \tag{48}$$

where

$$\Gamma_{i,j}^{e} = \int\limits_{V_e} \frac{1}{(\sigma_e + i\omega\varepsilon_e)^2} \begin{pmatrix} \frac{\partial\phi_i}{\partial y}\frac{\partial\phi_j}{\partial y} + \frac{\partial\phi_i}{\partial z}\frac{\partial\phi_j}{\partial z} & -\frac{\partial\phi_i}{\partial y}\frac{\partial\phi_j}{\partial x} & -\frac{\partial\phi_i}{\partial z}\frac{\partial\phi_j}{\partial x} \\ -\frac{\partial\phi_i}{\partial x}\frac{\partial\phi_j}{\partial y} & \frac{\partial\phi_i}{\partial x}\frac{\partial\phi_j}{\partial x} + \frac{\partial\phi_i}{\partial z}\frac{\partial\phi_j}{\partial z} & -\frac{\partial\phi_i}{\partial z}\frac{\partial\phi_j}{\partial y} \\ -\frac{\partial\phi_i}{\partial x}\frac{\partial\phi_j}{\partial z} & -\frac{\partial\phi_i}{\partial y}\frac{\partial\phi_j}{\partial z} & \frac{\partial\phi_i}{\partial x}\frac{\partial\phi_j}{\partial x} + \frac{\partial\phi_i}{\partial y}\frac{\partial\phi_j}{\partial y} \end{pmatrix} dv,$$

$$i, j = 1, \cdots, 8. \tag{49}$$

The finite element magnetic integral Jacobian equations (41)-(45) and finite element magnetic differential variation equation (47)-(49) will be assembled to construct a global integral and local differential inversion algorithm in the following next section of the parallel GILD algorithm.

REGULARIZING METHOD

Tikhonov regularizing method

Because the first type magnetic integral equation (14) for the electric conductivity and permittivity is essentially ill-posed, the Tikhonov regularizing method must be used (Tikhonov et al., 1977) to make a stable inversion.

The discrete nonlinear regularizing optimization of (15) will be

$$\left\| H_{data} - H_{model} \right\|^2 + \alpha \left(R(\sigma + i\omega\varepsilon), \sigma - i\omega\varepsilon \right) = \min . \tag{50}$$

Where, the regularizing operator R is a symmetry positive definite operator, the $(\cdot, \cdot)$ is the complex inner product.

Define

$$\begin{aligned} &\left((\Lambda + I) (\sigma + i\omega\varepsilon), (\sigma - i\omega\varepsilon) \right) \\ = &\int_{V_s} \left\{ \left[\left(\tfrac{\partial \bar{\sigma}}{\partial x} \right)^2 + \left(\tfrac{\partial \bar{\sigma}}{\partial y} \right)^2 + \left(\tfrac{\partial \bar{\sigma}}{\partial z} \right)^2 \right] + \omega^2 \left[\left(\tfrac{\partial \bar{\varepsilon}}{\partial x} \right)^2 + \left(\tfrac{\partial \bar{\varepsilon}}{\partial y} \right)^2 + \left(\tfrac{\partial \bar{\varepsilon}}{\partial z} \right)^2 \right] + \sigma^2 + \omega^2 \varepsilon^2 \right\} dv, \end{aligned} \tag{51}$$

where $\tilde{\sigma}$ and $\tilde{\varepsilon}$ are linear continuous and piecewise smooth fitting functions based on the σ and ε, respectively, by Kraft (1990) and Xie and Li (1979).

We choose $R = \Lambda + I$ as a regularizing operator and use the modified Gauss-Newton iterative method to solve the regularizing optimization equation (50). The iteration scheme is as follows

$$\begin{aligned} &\left[\Im^{h}{}_{\ell,l}^{T} \Im^{h}{}_{\ell,l} + \alpha R \right] \delta(\sigma + i\omega\varepsilon) \\ = &-\Im^{h}{}_{\ell,l}^{T} \Big[H_{d,l}(r_\ell) - H_{b,l}(r_\ell) + \int_{V_s} \nabla_{r'} g(r_\ell, r') \times \tfrac{(\sigma-\sigma_b) + i\omega(\varepsilon - \varepsilon_b)}{\sigma + i\omega\varepsilon} \left(\nabla_{r'} \times H_l{}^h - J_{c_l} \right) dr' \\ &- \int_{V_s} \nabla_r \times G_s^E (r_\ell, r') \tfrac{(\sigma-\sigma_b) + i\omega(\varepsilon - \varepsilon_b)}{\sigma + i\omega\varepsilon} \left(\nabla_{r'} \times H_l{}^h - J_{c_l} \right) dr' \Big] \\ &- \alpha R (\sigma + i\omega\varepsilon), \end{aligned} \tag{52}$$

where $\Im^h_{\ell,l}$ is the finite element approximation of the Jacobian operator $\Im_{\ell,l}$ by (16). The approximate Jacobian operations $\Im^h_{1,\ell,l}$ and $\Im^h_{2,\ell,l}$ are defined by (42)-(45).

Optimum regularizing parameter α

The regularizing parameter, α, is very important in the regularizing approach. The optimum regularizing parameter α has to be chosen for high resolution imaging.

Let H_{exact} be the exact measured data, H_{data} be the field measured data with noise, H_{emodel} be the exact model data, and H_{model} be the numerical model data, we have

$$\|H_{exact} - H_{data}\| \leq \delta, \tag{53}$$

$$\|H_{emodel} - H_{model}\| \leq \beta, \tag{54}$$

From optimization of (50) and definition of the regularizing operator, $R = \Lambda + I$ in (51), for a given α, the $H_{data} - H_{model}$ and $(R(\sigma + i\omega\varepsilon), \sigma - i\omega\varepsilon)$ can be calculated. Therefore

$$f(\alpha) = \|H_{data} - H_{model}\|^2, \tag{55}$$

$$g(\alpha) = (R(\sigma + i\omega\varepsilon), \sigma - i\omega\varepsilon), \tag{56}$$

and

$$h(\alpha) = \|H_{data} - H_{model}\|^2 - \delta^2 - \beta^2 \tag{57}$$

are functions of α.

It can be proven that $f(\alpha)$ is a continuous and almost monotonic non-decreasing function, $g(\alpha)$ is a continuous and almost monotonic non-increasing function of α, and $h(\alpha)$ is a continuous and almost monotonic function. The minimum root of (57) will be an optimum regularizing parameter by Yagola (1980). Xie et al. (1987) proved that the regularizing solution is convergent when α goes to zero.

In the nonlinear 3D EM inversion for practical data, δ is a physical system data noise bound and β is a numerical discrete error bound. The parameter δ can be estimated by statistics data analysis and β can be estimated by numerical analysis. The δ=0 is for synthetic data. For given noise bounds, δ and β, because the discrepancy function $h(\alpha)$ is continuous and almost monotonic, we use the quasi-Newton and bisection mixed method to find the optimum regularizing parameter.

A weaker regularizing method

A weaker regularizing method is used for the ill posed variation discrete equation (47). We rewrite the (47) as

$$\Gamma \begin{bmatrix} \delta\sigma \\ \delta\varepsilon \end{bmatrix} = \delta D. \tag{58}$$

The matrix Γ will be decomposed into the

$$\Gamma = PSQ \tag{59}$$

where S is diagonal matrix with the singular values of Γ, the P and Q are orthonormal matrices. The weaker regularizing solution of (47) is

$$\begin{bmatrix} \delta\sigma \\ \delta\varepsilon \end{bmatrix} = Q^T \left(S^2 + \beta I\right)^{-1} SP^T \delta D, \tag{60}$$

where β is a weaker regularizing parameter. A quasi-optimality approach by Leonov (1978) is used to find an optimum weaker regularizing parameter β.

PARALLEL GILD MODELING AND INVERSION ALGORITHM

In the preceding sections, we have described two systems, integral equation system and differential equation system, for the electromagnetic modeling and inversion. A question is why do we need two systems for the modeling and inversion? A new parallel global integral and local differential decomposition algorithm, GILD, for the modeling and inversion is presented in this section.

The conventional nonlinear inversion using the Gauss-Newton iteration

In the conventional nonlinear inversion using the Gauss-Newton iteration, the algorithm process is that (1) For giving conductivity, using finite element or finite difference scheme to solve Maxwell differential equation with an artificial absorption boundary condition to obtain the EM filed. (2) Solving a discrete norm equation of the regularizing optimization of the first type integral equation to update the electric conductivity. (3) The step (1) and (2) constructed the Gauss-Newton iteration for the conventional nonlinear inversion. The regularizing Gauss-Newton nonlinear inversion is a robust approach, but the limitations are: (1) Along the iterations, the inaccurate reflection error of the absorption boundary condition in the forward modeling enters the inversion domain as numerical noise that will cause low resolution; (2) the discrete integral equation in the inversion produces an ill-posed larger full matrix which is difficult or impossible to invert and store. A new GILD EM modeling and inversion algorithm is developed to overcome these limitations of the conventional nonlinear inversion.

New GILD modeling and nonlinear inversion

For simplicity, we used a rectangular mesh for modeling and inversion. The unknown magnetic field is defined on the set of the nodes for modeling. The unknown electric conductivity and permittivity are defined on the set of the cells for inversion. The new GILD modeling and inversion method consists of three steps: First, in (A) of Fig.1, the domain is decomposed into a subdomain CSI with white cells □ and a subdomain $CSII$ with dark cells ■ . This decomposition is called a cells-decomposition. The cells-decomposition should satisfy the following requirements: (1) the subdomain CSI should include the boundary of the domain; (2) the subdomain CSI should be a logical boundary of the subdomain $CSII$; (3) the subdomain $CSII$ can be decomposed into $2^p \times 2^q \times 2^r$ subdomains for 3D problem or $2^p \times 2^q$ subdomains for 2D problem, the p, q, r are integer. We used $2^2 \times 2^2$ 2D cells-decomposition to explain the GILD algorithm. The cells-decomposition induced a nodes-decomposition of the whole nodes of the domain, NSI and $NSII$. The subdomain NSI is the set of the boundary nodes ▪ and internal nodes •, i.e., the set of the nodes on the CSI. The subdomain $NSII$ is the set of the internal circle nodes o , i.e., the set of the inside nodes of $CSII$. Second, suppose that the electric conductivity σ and permittivity ε are obtained by the previous iterative step, the discrete magnetic integral equation (29) on the boundary nodes and the discrete magnetic differential equations (35) on the internal nodes of domain will be coupled to construct a complete equation system for the discrete magnetic field. The nodes-decomposition can be used for solving the modeling equations. Third, after obtaining the magnetic field, the global discrete magnetic Jacobian volume integral equation with the stronger regularizing (50) on cells of CSI and the local discrete magnetic Jacobian differential equations with the weaker regularizing (58) on cells of $CSII$ will be coupled to construct a complete equation system for updating the electric conductivity and permittivity. The cells-decomposition can be used for solving the equation system for updating parameters. The second step and third step are used to construct a loop of the parallel GILD Gauss-Newton iteration. If the residual of the misfit between the model field and the measured field data less than the giving tolerance then the iteration will be stop, otherwise the iteration should be running continuously.

The second step of GILD for magnetic field

The unknown magnetic field is defined on the set of the nodes for modeling. The discrete magnetic integral equation (29) - (32) only is built on the nodes ▪ of the boundary, i.e., the r_i in (30)-(31) are coordinate of the boundary nodes ▪ in (A) of Fig. 2,

$$IK_{B,B}H_B + IK_{B,D}H_D = S_B, \tag{61}$$

where H_B is the discrete magnetic field vector on the boundary nodes, H_D is the discrete magnetic field vector on the nodes in the internal domain, S_B is the discrete source term on the boundary, the matrices, $IK_{B,B}$ and the $IK_{B,D}$, are full matrices from the discrete integral equation (29)-(32) on the boundary. The $IK_{B,B}$ is the relative block matrix from the boundary nodes to boundary nodes, the $IK_{B,D}$ is the relative block matrix from the boundary nodes to the nodes in the internal domain. On the internal nodes of the domain in (A) of Fig. 2, • and ∘, we used the discrete sparse matrix equation (36) of the magnetic differential equation (10),

$$DK_{D,B}H_B + DK_{D,D}H_D = S_D, \tag{62}$$

where the $DK_{D,B}$ and $DK_{D,D}$ are sparse matrices from the discrete differential equation, the $DK_{D,B}$ is the relative block matrix from the internal nodes to the boundary nodes, the $DK_{D,D}$ is the relative block matrix from the internal nodes to the internal nodes, S_D is the discrete source term on the internal nodes of the domain. The equation (61) and (62) are coupled to construct the complete equation system for the magnetic field. We used the following parallel GILD modeling algorithm based on the nodes-decomposition to solve this equation system.

Parallel GILD modeling algorithm

1. According to the nodes-decomposition, NSI and $NSII$, the discrete magnetic field is decomposed into the two sub-magnetic vectors, H_I and H_{II}. The H_I is the discrete magnetic field defined on nodes ▪ and •, in the NSI, the H_{II} is the discrete magnetic field defined on nodes, ∘, in the $NSII$ in (A) of Fig. 2.

2. By reorganizing the equations (61) and (62) using the nodes-decomposition, we have

$$K_{I,I}H_I + K_{I,II}H_{II} = S_I, \tag{63}$$

and

$$K_{II,I}H_I + K_{II,II}H_{II} = S_{II}, \tag{64}$$

where the $K_{I,I}$ is the relative block matrix from the nodes in NSI to the nodes in NSI, the $K_{I,II}$ is the relative block matrix from the nodes in NSI to the nodes in $NSII$, $K_{II,I}$ is the relative block matrix from the nodes in $NSII$ to the nodes in NSI, the $K_{II,II}$ is the relative block matrix from the nodes in $NSII$ to the nodes in $NSII$.

3. In (B) of Fig. 2, the subdomain $NSII$ can be decomposed into the $2^2 \times 2^2$ smaller subdomains, $NSII(l)$, $l = 1, 2, ..., 4^2$, there is the same number of internal nodes in each subdomain. In each subdomain $NSII(l)$, there is internal node ∘ in

$NSII$ and logical boundary nodes • in NSI. The matrix equation (64) is decomposed into the following 4^2 independent matrix equations about $H_{II}^{(l)}$,

$$K_{II,I}^{(l)} H_I^{(l)} + K_{II,II}^{(l)} H_{II}^{(l)} = S_{II}^{(l)}, \quad l = 1, 2, \cdots, 4^2. \tag{65}$$

The 4^2 CPU processor elements in the Massively Parallel computer can be used to solve the equations (65), in parallel, and to present the sub magnetic field vector $H_{II}^{(l)}$ as follows

$$H_{II}^{(l)} = -\left(K_{II,II}^{(l)}\right)^{-1} \left(S_{II}^{(l)} - K_{II,I}^{(l)} H_I^{(l)}\right), \quad l = 1, 2, \cdots, 4^2, \tag{66}$$

using the LDL^T decomposition, the conjugate gradient iteration (Varga, 1962, Jacobs, 1986, and Golub et al., 1989), or Lanzos method (Simon 1982, Simon and Wu 1998).

4. Upon substituting

$$H_{II} = \sum_{l=1}^{4^2} H_{II}^{(l)}, \tag{67}$$

into the equation (63), and made some arrangements, we have a reduced matrix equation on the subdomain NSI in (C) of Fig. 2

$$\mathrm{P}_I H_I = \Theta_I \tag{68}$$

5. By decomposing the internal nodes • in the (C) of the Fig. 2 into the four groups, in general, $2^{p-1} \times 2^{q-1}$ groups, we make a frame in each group ((D) of Fig. 2). Let NSI_I be a set of the internal nodes • on the frames and the boundary nodes ▪ , $(H_I)_I$ be the unknown magnetic field vector on the NSI_I, NSI_{II} be a set of the nodes • inside of the frames, $(H_I)_{II}$ be the unknown magnetic field vector on the NSI_{II} . The equation (68) will be rewritten as

$$(\mathrm{P_I})_{I,I} (H_I)_I + (\mathrm{P_I})_{I,II} (H_I)_{II} = (\Theta_I)_I, \tag{69}$$

and

$$(\mathrm{P_I})_{II,I} (H_I)_I + (\mathrm{P_I})_{II,II} (H_I)_{II} = (\Theta_I)_{II}, \tag{70}$$

where $(\mathrm{P_I})_{I,I}$, $(\mathrm{P_I})_{I,II}$, $(\mathrm{P_I})_{II,I}$, and $(\mathrm{P_I})_{II,II}$ are block matrices by reorganizing and splitting the matrix $\mathrm{P_I}$, $(\Theta_I)_I$ and $(\Theta_I)_{II}$ are split source terms from the source term Θ_I in (68).

6. The equation (70) is decomposed into the 4 equations

$$(\mathrm{P_I})^{(l)}_{II,I}(H_I)^{(l)}_{I} + (\mathrm{P_I})^{(l)}_{II,II}(H_I)^{(l)}_{II} = (\Theta_I)^{(l)}_{II}, \quad l = 1, 2, \cdots, 4. \tag{71}$$

The 16 PES is divided into the 4 groups, the 4 PES in each group is used to solve each equation of (71) and to present the $(H_I)^{(l)}_{II}$ as

$$(H_I)^{(l)}_{II} = -\left((\mathrm{P_I})^{(l)}_{II,II}\right)^{-1}\left((\Theta_I)^{(l)}_{II} - (\mathrm{P_I})^{(l)}_{II,I}(H_I)^{(l)}_{I}\right), \quad l = 1, 2, 3, 4, \tag{72}$$

in parallel, using the parallel *LDL* decomposition, or parallel conjugate gradient iteration, or parallel Lanzos method.

7. Upon substituting the

$$(H_I)_{II} = \sum_{l=1}^{4}(H_I)^{(l)}_{II} \tag{73}$$

into the (69), we have reduced equation on the reduced mesh ((E) of Fig. 2),

$$\mathrm{P}\,(\mathrm{P}_I)_I\,(H_I)_I = \Theta\,(\Theta_I)_I\,. \tag{74}$$

8. A multi-level parallel *LU* forward decomposition will be used for the smaller matrices equation (74) on *NSI* in (E) and to obtain a 2 × 2 double layered block matrix equation in (F) of Fig. 2. Using the parallel *LU* algorithm, the magnetic field on the double layered in (F) of Fig. 2 will be obtained. Finally, a multi-level parallel backforward processor from the nodes on the boundary to the nodes in the internal domain is used to obtain the magnetic field on all nodes of the domain.

The third step of GILD for updating parameters

1. The cells-decomposition

In the (A) of Fig. 1 and (A) of Fig. 3, by cells-decomposition, the cells in the whole domain are decomposed into the subdomain CSI and the subdomain $CSII$. The subdomain CSI is the set of white cells □, the subdomain $CSII$ is the set of dark cells ■ . The electric conductivity and permittivity increment vector $(\delta\sigma, \delta\varepsilon)$ is decomposed into the two sub vectors, $(\delta\sigma_I, \delta\varepsilon_I)$ and $(\delta\sigma_{II}, \delta\varepsilon_{II})$, the $(\delta\sigma_I, \delta\varepsilon_I)$ is the electric conductivity and permittivity vector defined on cells in the subdomain CSI, the sub vector $(\delta\sigma_{II}, \delta\varepsilon_{II})$ is the electric conductivity and permittivity vector defined on cells in the subdomain $CSII$.

2. A global discrete normal magnetic integral equation (52) on the subdomain CSI

Using the collocation finite element approximation of normal equation (52) on the cells of CSI, we have the following matrix equation.

$$\Gamma_{I,I} \left\{ \begin{matrix} \delta\sigma_I \\ \delta\varepsilon_I \end{matrix} \right\} + \Gamma_{I,II} \left\{ \begin{matrix} \delta\sigma_{II} \\ \delta\varepsilon_{II} \end{matrix} \right\} = DH_I, \tag{75}$$

where $\Gamma_{I,I}$ and $\Gamma_{I,II}$ are finite element discrete submatrices of (52) on CSI, The DH_I is data on CSI.

3. A local discrete variation magnetic differential equation on the subdomain $CSII$.

In (B) of Fig. 3, the subdomain $CSII$ can be decomposed into the 4^2 sub-cubic domains, each sub-cubic domain has same number of the internal cells ■ in $CSII$ and logical boundary cells □ in CSI. In each sub-cubic domain, by using the Garlekin finite element approximation of variation differential equation (47) on the cells ■ , we have 2 block matrix equations

$$\Gamma^{(l)}_{II,I} \left\{ \begin{matrix} \delta\sigma^{(l)}_I \\ \delta\varepsilon^{(l)}_I \end{matrix} \right\} + \Gamma^{(l)}_{II,II} \left\{ \begin{matrix} \delta\sigma^{(l)}_{II} \\ \delta\varepsilon^{(l)}_{II} \end{matrix} \right\} = DH^{(l)}_{II}, l = 1, 2, ..., 4^2, \tag{76}$$

where $\Gamma_{II,I}{}^{(l)}$ and $\Gamma_{II,II}{}^{(l)}$ are finite element discrete matrices of (47) with the weaker regularizing, the $DH_{II}{}^{(l)}$ are data term on $CSII$.

The sparse matrix equations (76) are independent of each other and have the same size and structure. We use 4^2 CPU processor elements in the Massively Parallel computer to solve equations (76) and to present the local the electric conductivity and permittivity increment vector, in parallel,

$$\begin{Bmatrix} \delta\sigma_{II}^{(l)} \\ \delta\varepsilon_{II}^{(l)} \end{Bmatrix} = \left(\Gamma_{II,II}^{(l)}\right)^{-1} DH_{II}^{(l)} - \left(\Gamma_{II,II}^{(l)}\right)^{-1} \Gamma_{II,I}^{(l)} \begin{Bmatrix} \delta\sigma_{I}^{(l)} \\ \delta\varepsilon_{I}^{(l)} \end{Bmatrix}, l = 1, 2, ..., 4^2, \tag{77}$$

where $\left(\Gamma_{II,II}^{(l)}\right)^{-1}$ is generalized inversion of the $\Gamma_{II,II}$ with weaker regularizing in (60) (Xie et al., 1987) and (Lee and Xie, 1993).

4. Upon substituting

$$\begin{pmatrix} \delta\sigma_{II} \\ \delta\varepsilon_{II} \end{pmatrix} = \sum_{l=1}^{4^2} \begin{pmatrix} \delta\sigma_{II}^{(l)} \\ \delta\varepsilon_{II}^{(l)} \end{pmatrix} \tag{78}$$

into the (75), we have

$$\Pi \begin{bmatrix} \delta\sigma_I \\ \delta\varepsilon_I \end{bmatrix} = T \begin{bmatrix} DH_I \\ DH_{II} \end{bmatrix} \tag{79}$$

where Π and T are smaller full matrices on the CSI.

5. A parallel LU decomposition or parallel preconditioned biconjugate iteration algorithm (Golub et al., 1989) will be used to solve the smaller full matrices equation in CSI, (79), in parallel. Finally, a parallel backforward processor is used to obtain $\delta\sigma$ and $\delta\varepsilon$ on the cells of the $CSII$ by (77). (Xie and Zuo, 1991, Xie and Li, 1988, and Xie et al., 1995c).

In the parallel program, the shared data, the shared do loops, and message passing interface (MPI) are used for communication and distribution of subdomain field data and matrix data on a massively parallel computer. In this parallel program, distribution of the jobs in the parallel processing is uniform and the parallel arrangement is done appropriately. The new global integral and local differential parallel inversion has been tested in the multiple processor of the Special Parallel Processing (SPP) in the CRAY-A.NERSC.GOV and the Massively Parallel computer T3D. The parallel effective rate is 80% to 96%. The description of the new parallel GILD modeling and inversion algorithm is presented in a Lawrence Berkeley National Laboratory technology report by Xie and Li (1997).

ELECTRIC FIELD CALCULATION

In the preceding sections, the calculation method of the magnetic field in the domain V_s is described. The magnetic field outside of the domain V_s is calculated by using the discrete magnetic integral representation (28), where r is located outside of the domain V_s and r' is in the domain V_s. For completeness, the finite element approximation of the electric field is presented in this section.

Electric field approximation in the domain V_s

In the point r inside of each element $V_e \subseteq V_s$, the finite element approximation of the electric field is calculated by

$$E^h(r) = \frac{1}{\sigma_e + i\omega\varepsilon_e} \nabla \times H^h, \tag{80}$$

where H^h is presented by (22). In the point r on the interface boundary plane between the elements, for example, element e1 and element e2, the finite element approximation of the electric field is calculated by

$$E^h(r)\,|_t = 0.5 \left\{ \left(\frac{1}{\sigma_{e1} + i\omega\varepsilon_{e1}} \nabla \times H^h_{e1} \right) |_t + \left(\frac{1}{\sigma_{e2} + i\omega\varepsilon_{e2}} \nabla \times H^h_{e2} \right) |_t \right\}, \tag{81}$$

and

$$E^h(r)\,|_{nl} = \left(\frac{1}{\sigma_{el} + i\omega\varepsilon_{el}} \nabla \times H^h_{el} \right), l = 1, 2, \tag{82}$$

where $|_t$ denotes a tangent component and $|_n$ denotes a normal component with respect to the interface boundary plane. Similarly, the formulas for electric field on the edge and corner of the element can be written.

Electric field approximation outside of the domain V_s

The electric field approximation outside of the domain V_s is calculated by the following discrete integral representation

$$\begin{aligned} E^h(r) &= E_b^h(r) \\ &- i\omega\mu \sum_{e=1}^{M} \left\{ \tfrac{(\sigma_e-\sigma_{be})+i\omega(\varepsilon_e-\varepsilon_{eb})}{\sigma_e+i\omega\varepsilon_e} \int\limits_{V_e} G_b^E(r,r') \left(\nabla \times H^h - J_e\right) dr' \right\}, \end{aligned} \tag{83}$$

Electric field approximation on the boundary of the domain V_s

The electric field approximation on the boundary of the domain V_s can calculated by using (83), or (81) and (82).

APPLICATIONS

The new 3D nonlinear magnetic integral inversion algorithm has been tested by using two synthetic models. Model 1 in (A) of Fig. 4 is a (90m, 90m, 80m) cubic conductor of 0.1 S/m conductivity that includes a (30m, 30m, 50m) cubic conductor of 0.25 S/m conductivity inside. The geometry of model 2 in (B) of Fig. 4 is the same as model 1, the conductivity in the outer part of the cube is 0.25 S/m, and the conductivity of the inner cube is 0.1 S/m. The permittivity is ε_0. The 18 frequencies employed are 10, 18, 31, 55, 96, 180, 300, 530, 938, 1658, 3000, 5000, 10000, 16000, 20000, 28000, 38000, and 50000 Hz. 64 vertical magnetic dipole sources on the surface, and 768 receivers on the surface were used to create synthetic surface data by solving the forward finite element discrete magnetic integral equation. The geometry pattern of the 1 source and 12 receivers is shown in (B) of Fig. 1. At each receiver point, the three magnetic components, Hx, Hy, and Hz are measured. The amplitude of the vertical magnetic surface data of the model 1 excited by the vertical magnetic source in the center of the surface is shown in Fig. 5 with a solid line. The total field, incident field, and scattering field for 50000 Hz are plotted in frames (1.1), (1.2), and (1.3), respectively; the total field, the incident field, and the scattering field for 10000 Hz are plotted in frames (2.1), (2.2), and (2.3), respectively; the total field, the incident field, and the scattering field of 10 Hz are plotted in frame (3.1), (3.2), and (3.3), respectively. The phase of the vertical magnetic surface data of the model 1 excited by the vertical magnetic source in the center of the surface is shown in Fig. 6 with a solid line. In testing of the new inversion, the background conductivity was assumed known (0.05 S/m), the above model was imbedded in the large cubic domain [-90m, 90m; -90m, 90m; 0,120m] and the initial conductivity is 0.05 S/m. The model is divided into the $35 \times 35 \times 25 = 30625$ cells and 33696 nodes. The 16 CPU processors and 33 minutes wall time in the the Cray-C90 were used to run the inversions for the synthetic data. The new 3D nonlinear electromagnetic inversion is stable convergent and the parallel efficiency is 90%. The normalized residual going down to 1.0e-3 from 1.0 after 18 iterations and the conductivity image were obtained. The initial regularizing parameter is 1.0^{-3} for two models, the optimization regularizing parameter is 1.07639X10-5 for model 1 and 1.17856X10-5 for model 2. The cross section of the conductivity image of model 1 is shown in (C) and the conductivity image of model 2 is shown in (D) of Fig. 4. The amplitude and phase of the vertical magnetic field obtained by the inversion of the model 1 are shown in Fig. 5 and Fig. 6 with a dashed line. For comparison with the conventional electric integral inversion, we used our electric integral inversion program for the above models. The model is divided into the $23 \times 23 \times 21 = 11109$ cells and 12672 nodes. The one CPU processor and 39 hours in CRAY-C90 were used to run inversion for each model synthetic data. After 24 iterations, the normalized residual going down to 1.0e-3 from 1.0. The initial regularizing parameter is 1.0^{-3} for two models, the optimization regularizing parameter is 1.8346X10-4 for model 1, and 1.7578X10-4 for model 2. The results are shown in (E) and (F) of Fig. 4. We used EPA Rocky Mountain Arsenal field data to test the 3-D new nonlinear inversion and the traditional electric integral inversion.

The data configuration was described in Lee et al. (1996). The twelve (12) transmitters on the surface were used. For each transmitter, the vertical magnetic fields are available at five location ((B) of Fig. 1); 11 frequency data have been selected for the inversion. These frequencies were 36, 73, 164, 346, 746, 1602, 3458, 7445, 16036, 25410, and 40280Hz. The cells of the inversion domain were 46x46x46=97336. After 18 iterations, the normalized residual was decreased to 0.012 from 1.0 and the iterative processes was stable. We used 64 PES and 56 minutes wall time with parallel rate 89% in the T3D to solve the nonlinear inversion. The resistivity imaging using the new 3D inversion were shown by five plots on left size of Figure 7. The one in the middle with Y=0 m represents an east-west cross section bisecting the survey area. This imaging is consistent with that indicated by the result of 1-D inversion. The next two cross sections Y=30 m and Y=60 m to the south, the cross section at Y=-30 m and Y=-60 m to the north. These imaging show the 3D high resolution conductivity structures. The five imaging in the right side of Fig. 7 were results of the traditional nonlinear electric integral inversion, the cells are 31x31x31= 29791. The one CPU processor and 87 hours in CRAY-C90 were used to run this job. After 10 iterations, the normalized residual was decreased to 10^{-1} from 1.0. The figure shows five conductivity cross sections. We compared the imaging on left and imaging on the right. It is obvious that the imaging using the new 3D nonlinear inversion has a high resolution. In Fig. 8, the high resolution resistivity imaging using the new 3D nonlinear and the crosshole field data is shown. The two resistivity imaging of the before and after steam injection are shown in plots (a) and (b), respectively. The (c) shows a differences imaging made by substracting the two images (a) and (b). Based on the difference in the imaging before and after the steam injection, how and where the steam was moving that can be shown clearly. The field data is from the steam injection experiment in the Bakersfield oil field in central California by Dr. Michael Wilt. The 32 x 18 crosshole source receiver pairs and single frequency of 5K Hz data is used for inversion. The distance between crosshole is 54 m. We used 61x21x80

=102480 cells for inversion domain. We used 64 CPU processor elements (PEs) and 2.5 hours wall time in the massively computer T3D to run the imaging job using the new 3D nonlinear inversion code. After 28 iterations, the normalized residual was decreased to 0.026 from 1.0. The reasonable imaging was obtained that is shown in Fig. 8. In this paper, only conductivity imaging is presented.

CONCLUSIONS

In this paper, a new 3D parallel GILD EM modeling and nonlinear inversion algorithm is developed. The new 3D modeling and nonlinear inversion has been tested by using synthetic data and field data obtained from environmental sites and oil field. We obtained very good imaging (Fig. 4) for synthetic data and a reasonable subsurface EM imaging (Fig. 7 - Fig. 10) for practical data. By comparison between (C) and (E), (D) and (F) of Fig. 4, the new magnetic integral inversion is better than the traditional electrical integral equation for 3D electric conductivity inversion. The new nonlinear inversion method in this paper is available for $\omega \geq \omega_0 > 0$. For the magnetic permeability inversion, we used an electric integral equation (11) (Li and Xie, 1997). It is interesting to note that the new magnetic integral equation (8) is a dual integral equation of the electric integral equation (11). The benefits of the new magnetic integral equation for modeling and inversion are: (a) The magnetic field in (8) is continuous when electric conductivity is discontinuous, which is convenient for using the finite element method, (b) The kernel function in equation (8) is integrative weakly singular, (c) There is a parameter relative difference term, $\frac{\delta\sigma + i\omega\delta\varepsilon}{\sigma + i\omega\varepsilon} \cong \delta \log(\sigma + i\omega\varepsilon)$, that is the natural logarithmic scale inversion, and (d) The magnetic integral equation (8) and magnetic differential equation (10) can be consistently assembled to construct a new global integral and local differential parallel algorithm. The discrete matrix of the differential equation for modeling is sparse, but the inconvenient artificial radiation or absorption boundary conditions must be imposed. A merit of the integral equation approach for modeling and inversion is that the artificial boundary condition is not needed, but its discrete matrix is full. The new parallel GILD algorithm has both the merits of a local sparse matrix and no artificial boundary condition needed.

Advantages of new parallel GILD modeling and nonlinear inversion

The new GILD parallel modeling and nonlinear inversion algorithm is a new development of 3D nonlinear inversion. The algorithm is designed to overcome the shortcomings of the conventional inversion. The advantages of the GILD algorithm are: (1) using a new exact global volume or boundary integral equation (Xie et al. 1998) and local differential equation in the domain that reduces the numerical boundary noises and improves accuracy of the modeling and inversion; (2) using a new global integral and local differential decomposition in inversion that decompose the ill-posed full matrix into 4^n small sparse matrices and a smaller full matrix, greatly improved the ill-posed condition, and reduced computation time and storage requirements; (3) the GILD is a high performance parallel multiple hierarchy algorithm with parallel efficiency of 96%; (4) it minimized data communication between processors that is suitable for the architecture of the massively parallel computer T3E with distribution memory; (5) the GILD parallel algorithm can be widely useful to solve elliptic, parabolic, and hyperbolic modeling and inversion in the T3E massively parallel computer that will be a great benefit for expanding T3E's applications in science and engineering.

ACKNOWLEDGMENTS

The new 3D nonlinear magnetic integral inversion algorithm is supported by DOE Massively Parallel computer allocation. In particular, the authors are grateful to Professor P. D. Lax. and Professor Ting Lu in Courant Institute of NYU, Professor

Y. M. Chen in Stony Brook of SUNY, the SEG associate editor Dr. G. A. Newman, the reviewer Dr. A. P. Raiche, Dr. Habashy, T. M., Dr. Dr. Ellis, R. G., and an anonymous reviewer for their critical reviews , valuable suggestions for improvement. We are grateful to the assistant editor Kurt J. Marfurt , editor Larry R. Lines and former editor Sven Treitel for their encouragement The authors would like to thank Dr. Horst Simon and Dr. Kesheng John Wu n NERSC for their suggestions and help. The authors would like to thank Dr. Ki Ha Lee for his help and Dr. Christine Doughty and Dr. Janet S. Jacobson for their reviews and suggestions, Dr. Bruce Curtis and consultants of the National Energy Research Supercomputer Center, and Carol Taliaferro for their help. The authors would like to thank Dr. Michael Wilt for his crosshole data.

REFERENCES

Chen, Y. M. and Kim, T. G., 1995, A parallel algorithm for inverse scattering problems of Maxwell's equations on hypercubes: Proceedings of 3rd International Conference on Mathematical and Numerical Aspects of Wave Propagation, France, SIAM, Philadelphia, 635-643.

Ciarlet, P. G., 1978, The finite element method for elliptic problems: Amsterdam, North-Holland.

Ellis, R. G., 1995, Joint 3D EM inversion: Proceedings of International Symposium on Three-Dimensional Electromagnetics. Oct. 4-6, Schlumberger-Doll Research, Ridgefield, CT, USA, 307-323.

Golub, G. H., and Van Loan, C. F., 1989, Matrix computations: The Johns Hopkins Press, Baltimore, Maryland.

Habashy, T. M., Groom, R. W., and Spies, B. R., 1993, Beyond the Born and Rytov approximation: J. Geophysics, Res., v.10, 98-B2, 1759-1775.

Habashy, T. M., Oristaglio, M. L., and de Hoop, A. T., 1994, Simultaneous nonlinear reconstruction of two-dimensional permittivity and conductivity: Radio Sciences, v.29, 1101-1118.

Hohmann, G. W., 1975, Three-dimensional induced polarization and electromagnetic modeling: Geophysics, v.40, 309-324.

Jacobs, D. A. H., 1986, A generalization of the conjugate-gradient method to solve complex system: IMA Journal of Numerical Analysis, v.6, 447-452.

Kraft, Richard Betts, 1990, Splines through groups, Springer-Verlag, New York.

Lee, K.H. and Xie, G., 1993, A new approach to imaging with low-frequency electromagnetic fields: Geophysics, v.58, 780-796.

Lee, K.H., Xie, G., Hoversten, M., and Pellerin, L., 1995, EM imaging for environmental site characterization: Proceedings of International Symposium on Three-Dimensional Electromagnetics. Oct. 4-6, Schlumberger-Doll Research, Ridgefield, CT, USA, 483-490.

Leonov, A. S., 1978, On the choice of regularization parameters by means of the quasi-optimality and ratio criteria: Soviet Math. Dokl., 19, 537-540.

Li J. and Xie, G., 1998, A 3D cubic-hole element and its application in resistivity imaging. 3-D Electromagnetic Methods, Proceedings of the International Symposium on Three-dimensional electromagnetics in Schlumberger-Doll Research, 1995, P. 415-419. SEG book, P. 591-599. Editor, Oristaglio and Spies, to be published in September 1998.

Li, J., Lee, K. H., Javandel, I., and Xie, G., 1995, Nonlinear three-dimensional inverse imaging for direct current data: SEG 65th Annual International Meeting and Exposition, Expanded Abstracts, 250-253.

Li, J. and Xie, G. 1997, A New 3D magnetic permeability inversion: In preparation for LBNL report.

Mackie, R.L. and Madden, T.R., 1993, Three-dimensional magnetotelluric inversion using conjugate gradients: Geophysics, v.115, 215-229.

Nekut, A.G., 1994, Electromagnetic ray-trace tomography: Geophysics, v.55, 371-377.

Newman G. A., (1995), Crosswell electromagnetic inversion using integral and differential equations: Geophysics, v.60, 899-911.

Newman G. A. and Alumbaugh, D.L., 1995, 3-D massively parallel electromagnetic inversion: Proceedings of Progress in Electromagnetics Research Symposium, The University of Washington,324

Pellerin, L., Johnston, J.M., and Hohmann, G.W., 1993, Three-dimensional Inversion of Electromagnetic Data: SEG 63rd Annual International Meeting and Exposition, Expanded Abstracts, 360-363.

Raiche, A. P., 1974, An integral equation approach to three-dimensional

Simon, H. D., 1982, The Lanczos Algorithm for solving SLS. PhD thesis, UCB.

Tikhonov, A.N. and Arsenin, V.Y., 1977, Solutions to ill-posed problems: John Wiley and Sons, Inc.

Torres-Verdin, C. and Habashy, T.M., 1994, Rapid 2.5-D forward modeling and inversion via a new nonlinear scattering approximation: Radio Science v.29, 1051-1079.

Varga, R. S., 1962, Matrix iterative analysis: Prentice-Hall, Englewood Cliffs, NJ.

Weidelt, P., 1975, Electromagnetic induction in three-dimensional structures, J. Geophys., v.41, 85-109.

Wu, K. and Simon, H. D., 1997, A parallel Lanczos method for symmetric generalized eigenvalue problems, LBNL - 41284.

Xie, G., Li, J. and Zuo, D., 1997, 3D electromagnetic imaging using a new parallel GILD nonlinear inversion: Proceedings of SEG International Exposition and 67th Annual Meeting. 414-417.

Xie, G. and Li, J., 1997a, A new 3D parallel high resolution electromagnetic nonlinear inversion based on global integral and local differential decomposition: LBNL report, LBNL-40265.

Xie, G. and Li, J. 1997b, 3D extrapolating electromagnetic imaging, Proceedings of Progress in Electromagnetics Research Symposium, Cambridge, Massachusetts, 756

Xie, G., Li, J., and Lee, K. H., 1995a, New 3D nonlinear electromagnetic inversion: Proceeding of International Symposium on Three-Dimensional Electromagnetics. Oct. 4-6, Schlumberger-Doll Research, Ridgefield, CT, USA, 405-414.

Xie, G., Li, J., and Lee K. H., 1995b, Annealing regularization for high resolution geophysical tomography: Proceedings of 3rd SEGJ/SEG International Symposium on Geotomography, Nov. 8-10, Tokyo, Japan,102-109.

Xie, G., Lee, K.H., and Li, J.,1995c, A new parallel 3D numerical modeling of the electromagnetic field: SEG 63rd Annual International Meeting and Exposition, Expanded Abstracts, 821-824.

Xie, G. and Zou, Q, 1991, A parallel algorithm for solving the 3D inverse scattering problem: Computer Physics Communications, v.65, 320-326.

Xie, G. and Li, J. 1988, New iterative method for solving inverse scattering problem of 3-D wave equation: Science in China (English series A), v.31, 1195-1202

Xie, G., Li, J., and Chen, Y. M., 1987, Gauss-Newton-regularizing method for solving coefficient inverse problem of PDE and its convergence: J. of Computational Mathematics, v.5, 38-49.

Xie, G. and Chen, Y. M., 1985, A modified pulse-spectrum technique for solving inverse problems of two dimensional elastic wave equation: Applied Numerical Mathematics, v.1, 217-237.

Xie, G., 1981, An analysis of finite element method for the minimization of convex functionals: Acta Math. Appl. Sinica, v.3, 57-71.

Xie G. and Li, J., 1979, Stress Galerkin distribution in the finite element method. J. mathematical practice and recognization, vol. 7, no.2. 1979.

Xie, G., 1975, 3D finite element method in the elastic mechanics: Applied and Computational Mathematics, v.8, 28-48, (Chinese)

Yagola, A.G., 1980, On the choice of regularization parameter when solving ill-posed problems in reflexive spaces: USSR Comput. Maths. Math. Phys. v.20, 40-52, Printed in Great Britain, 1981, Pergamon Press Ltd.

Zhdanov, M. S. and S. Fang, 1996, 3-D quasi-linear electromagnetic inversion: Radio Sciences, v.31, 741-754.

Zhou, Q., Becker, A., and Morrison, H. F., 1993, Audio-frequency electromagnetic tomography in 2-D: Geophysics, v.58, 284-495.

FIGURES

FIG. 1. The new GILD domain decomposition and source pattern

FIG. 2. The GILD nodes-decomposition

FIG. 3. The GILD cells-decomposition

FIG. 4. Resistivity imaging of the 3D EM inversion for synthetic data

FIG. 5. Amplitude: solid line - magnetic field of modeling, dashed line - magnetic field of inversion

FIG. 6. Phase: solid line - magnetic field of modeling, dashed line - magnetic field of inversion

FIG. 7. Comparison between resistivity imaging using new 3D nonlinear inversion and the traditional electric integral nonlinear inversion

FIG. 8. Resistivity imaging using new 3D nonlinear inversion and the crosshole field data

FIG. 9. Parallel 3D GILD resistivity imaging using new 3D nonlinear inversion and the crosshole field data

FIG. 10. Parallel 3D GILD Resistivity imaging for VETEM field data

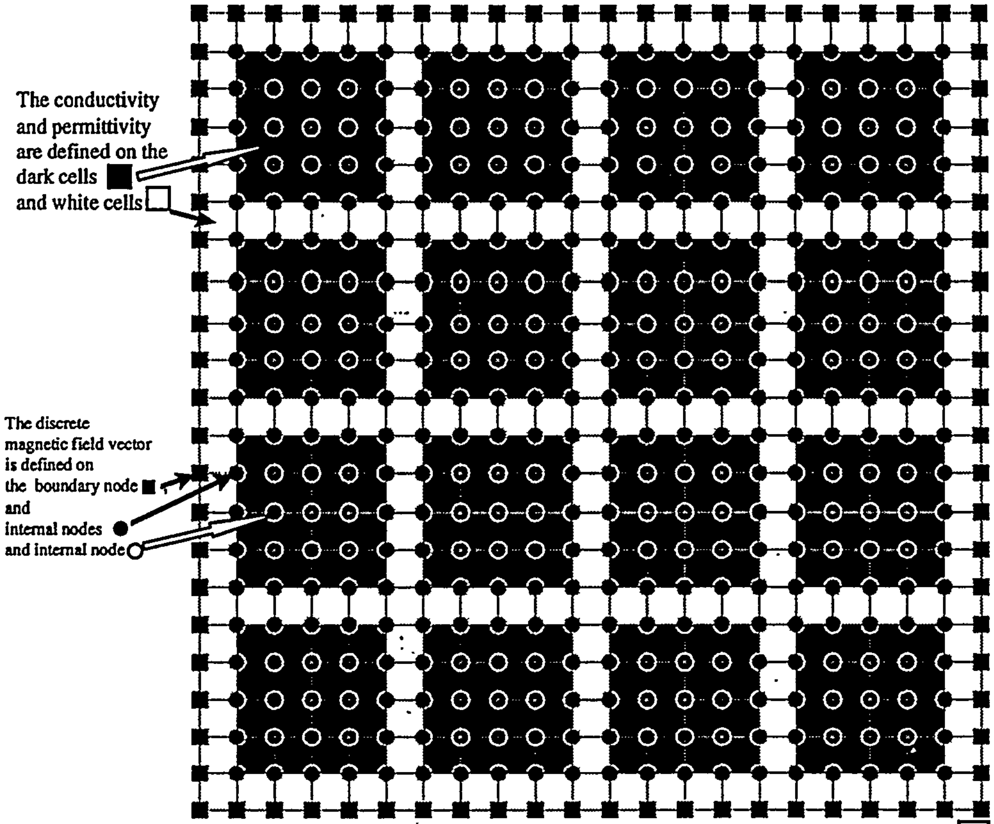

(A) The whole domain is decomposed in to the subdomain *CSI* that is set of the white cells □ and subdomain *CSII* that is set of the dark cells ■. The cells decomposition, *CSI* and *CSII* , induced a decomposition of whole nodes, the *NSI* and *NSII*. The *NSI* is set of the boundary nodes ■, and internal dot nodes ● that are nodes on the *CSI*, the *NSII* is a set of the nodes ○ that is the internal nodes of *CSII*.

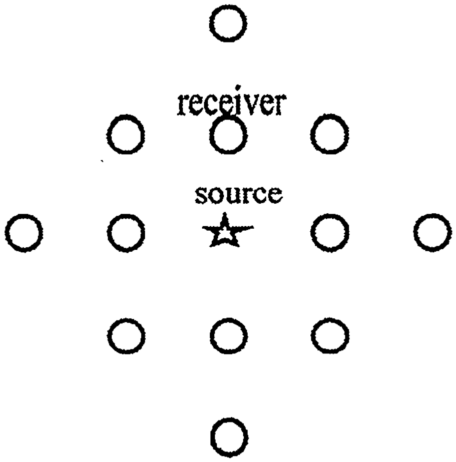

(B) The pattern of the 1 source and 12 receivers

Fig. 1 The new GILD domain decomposition and source-receiver pattern

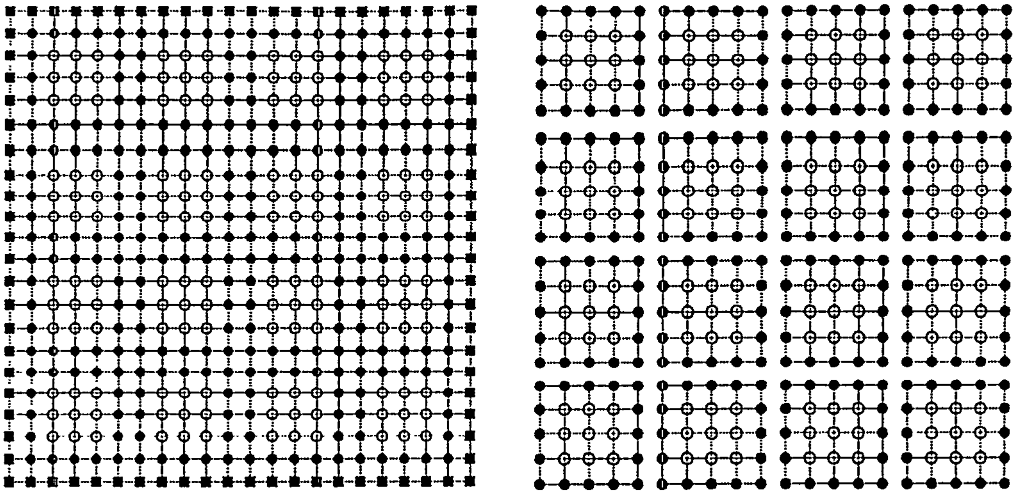

(A) The nodes of the whole domain is decomposed *NSI* and *NSII*, *NSI* is set of ■ and ●, and *NSII* is set of ○.

(B) The *NSII* is decomposed $4^2=16$ subdomains with internal ○. The 16 PES will be used to solve FEM sparse matrix eq. in each subdomain by LDL^T, in parallel

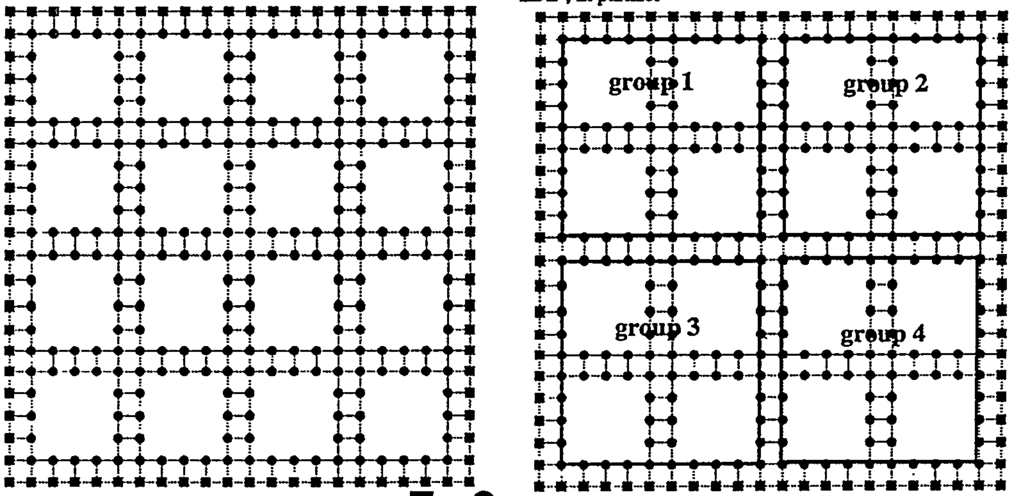

(C) A reduced matrix equation on the *NSI* with ■ and ●.

(D) The *NSI* is also decomposed into the $(NSI)_I$ with nodes ● on the frame and boundary node ■, and $(NSI)_{II}$ with nodes ● inside of frame. 4 x 4 PES group will be used solve 4 sparse matrix equations, in parallel

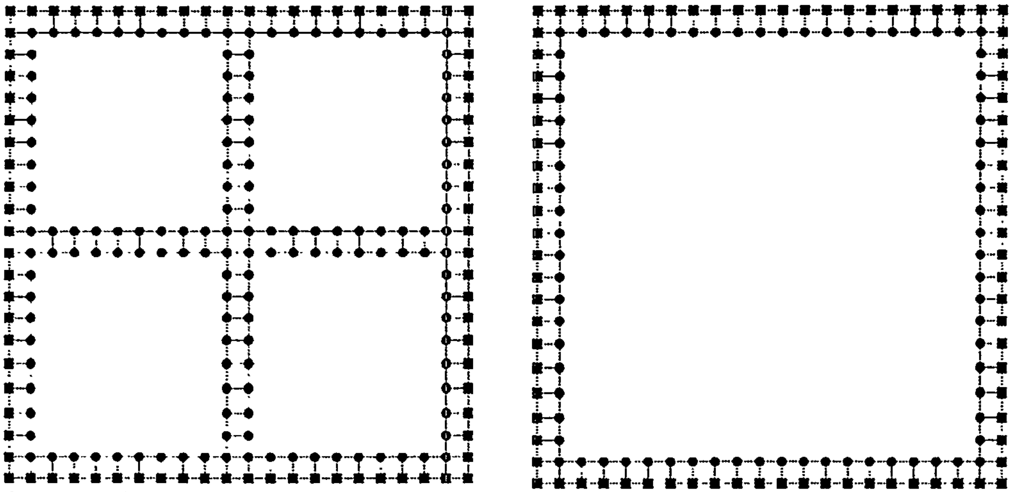

(E) A more reduced matrix equation on the reduced mesh.

(F) parallel LU algorithm is used to solve double layered matrix eq.

Fig. 2 The new GILD nodes-decomposition for modeling

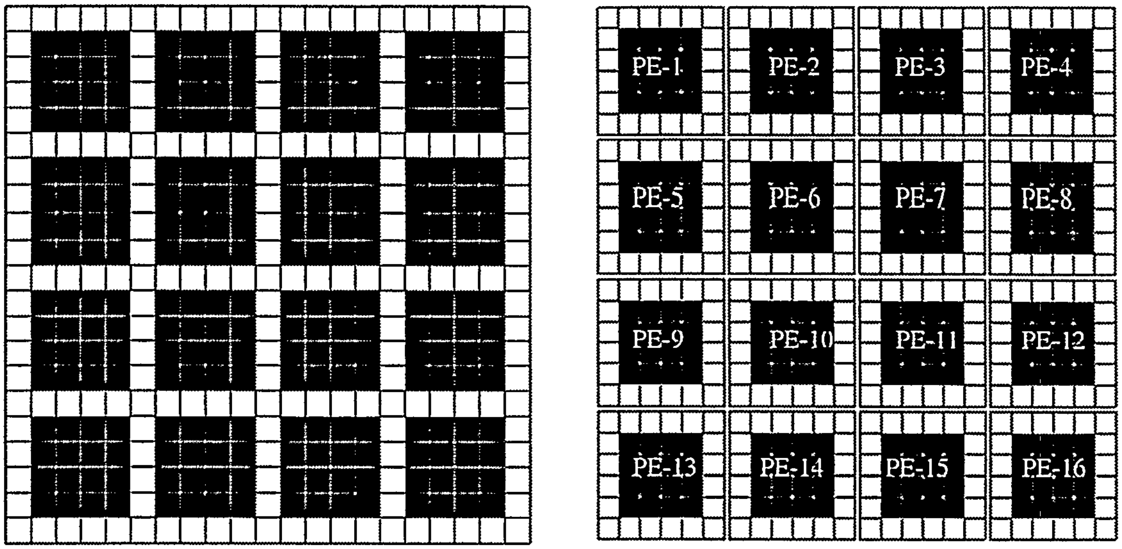

(A) The cells in whole domain is decomposed subdomain CSI with white cell ☐ and subdomain CSII with dark cell ■.

(B) The subdomain is also decomposed 4^2=16 sub domains with internal cells ■. 16 PES will be used to solve discrete variation differential eq. for increment of parameter in each sub domain, in parallel.

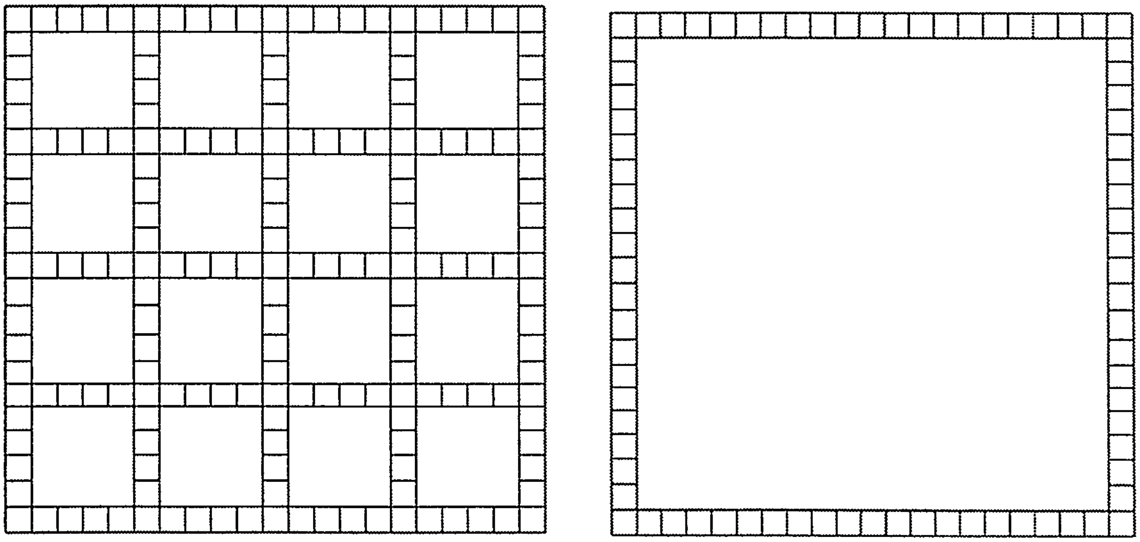

(C) A reduced matrix equation about increment of parameter on the *CSI.*

(D) Parallel multiple level *LU* decomposition will be used solve the reduced matrix eq from internal to boundary cells.

Fig. 3 The new GILD cells decomposition for inversion

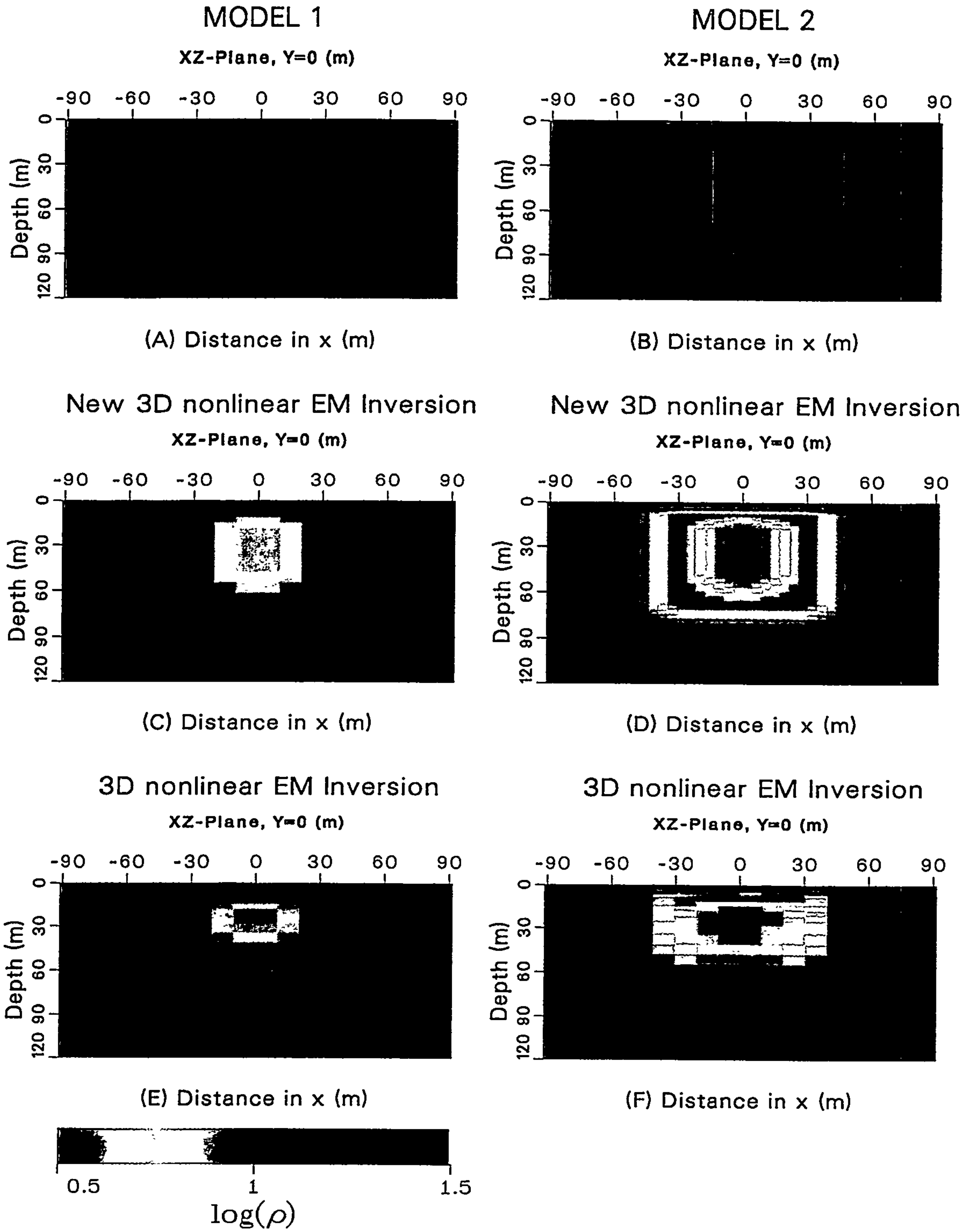

FIG. 4. Resistivity imaging of the 3D EM inversion for synthetic data

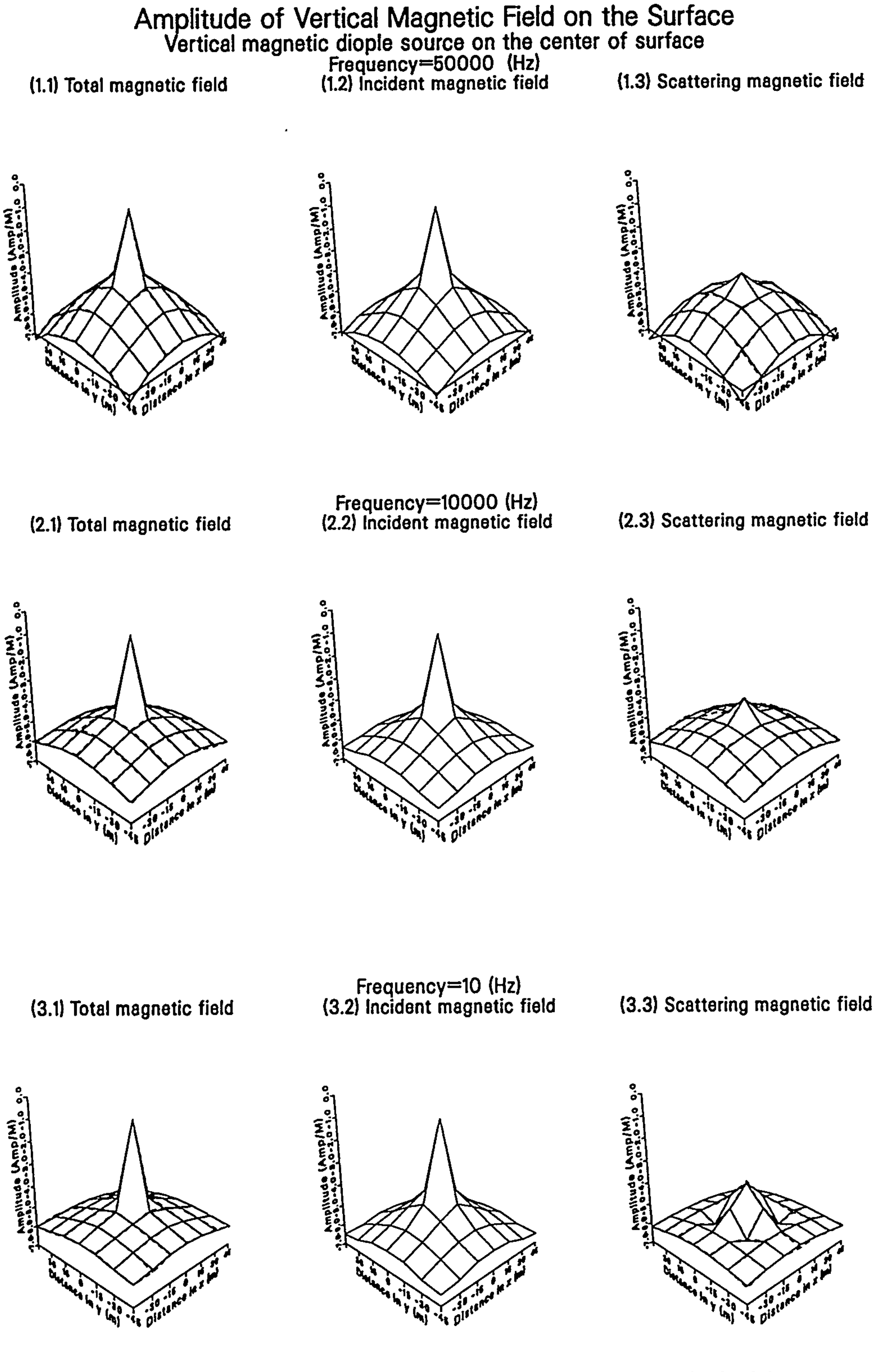

FIG. 5. Amplitude: solid line - magnetic field of modeling, dashed line - magnetic field of inversion

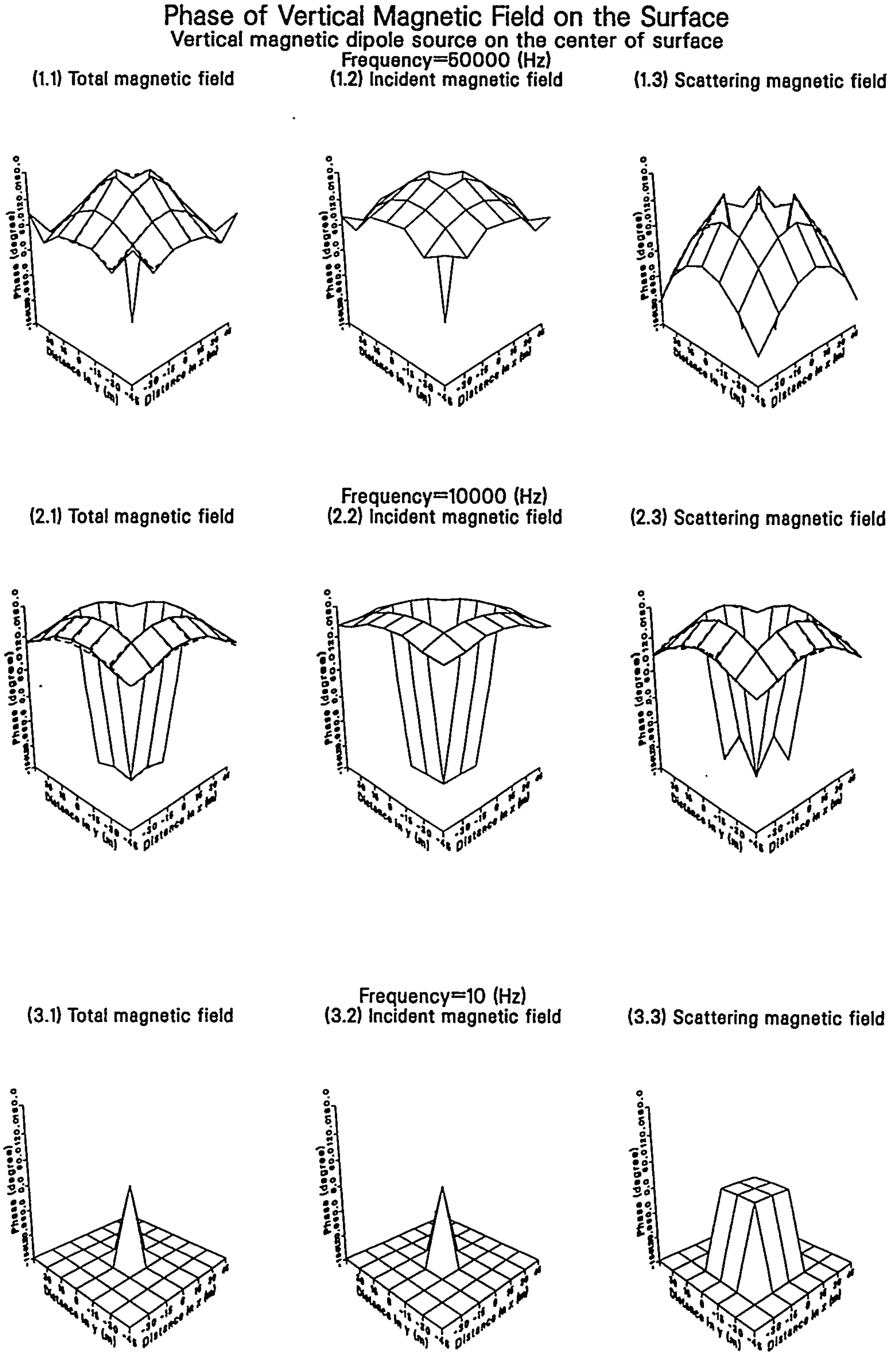

FIG. 6. Phase: solid line - magnetic field of modeling, dashed line - magnetic field of inversion

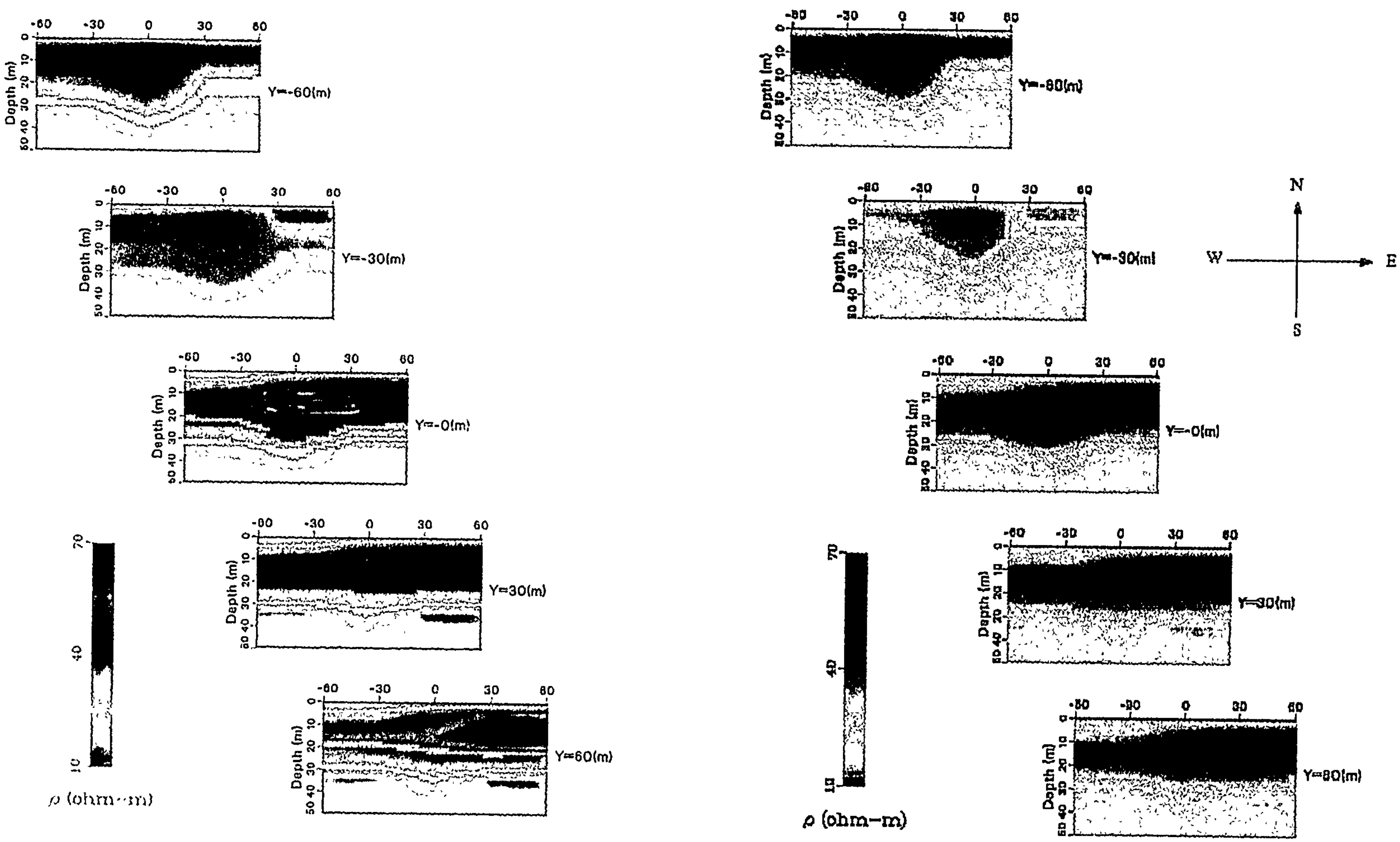

Resistivity imaging using new 3D GILD nonlinear inversion

Resistivity imaging using electric integral inversion

FIG. 7,, Comparison between resistivity imaging using new 3D nonlinear inversion and the tradition electric integral nonlinear inversion

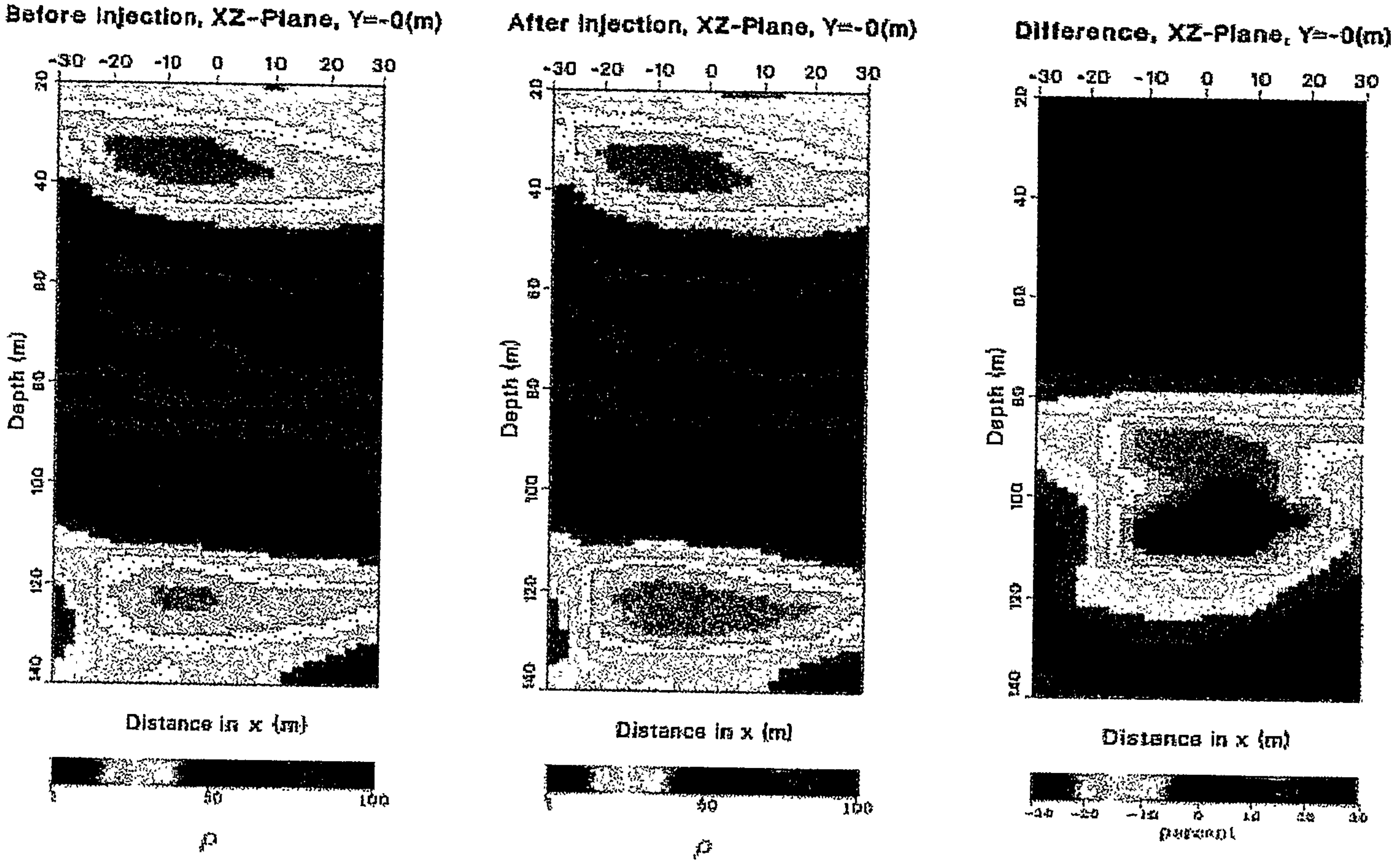

(a) (b) (c)

FIG. 8, Resistivity Imaging Of New 3D EM Nonlinear Inversion Using Crosshole Data

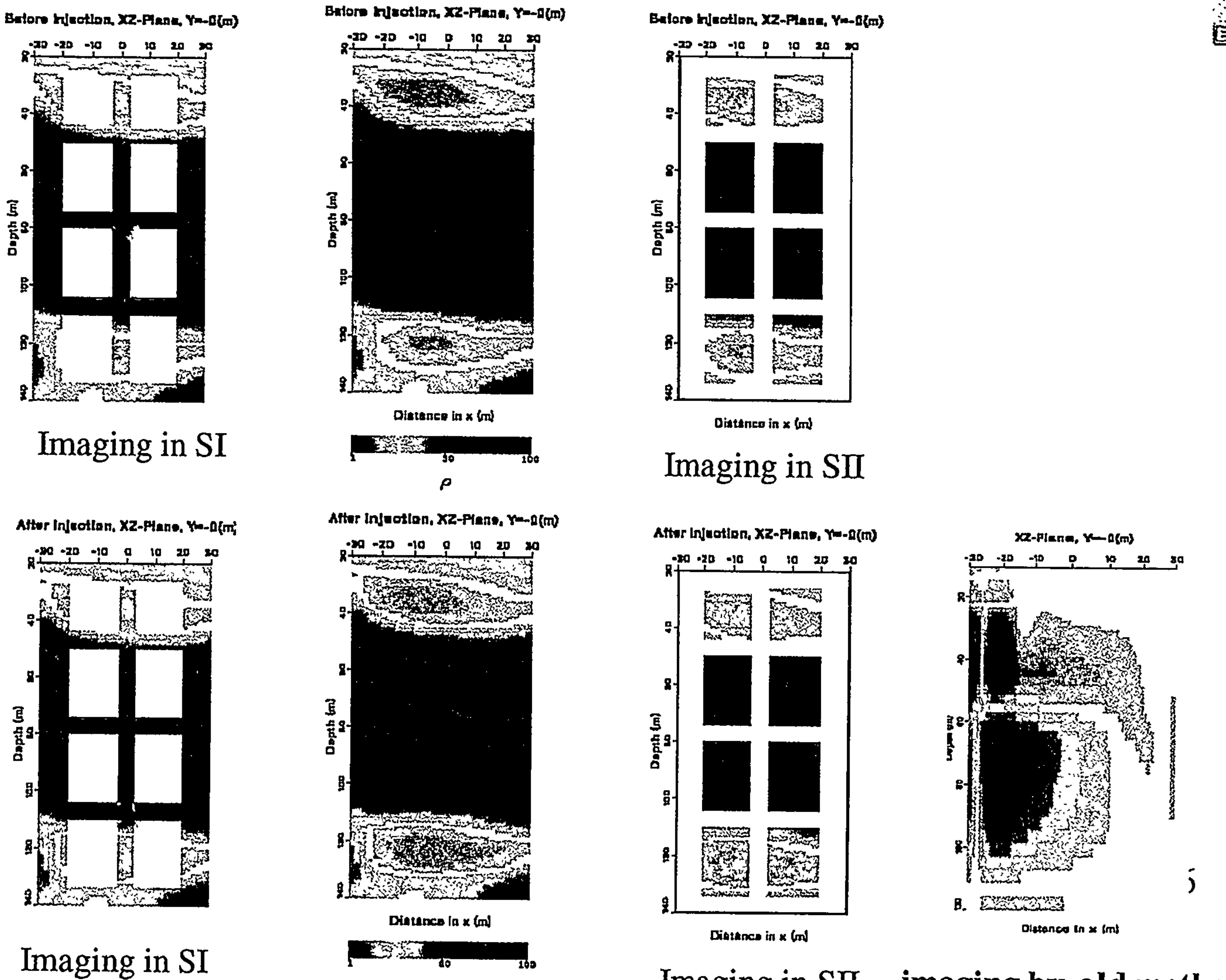

Imaging in SI

Imaging in SII

Imaging in SI

Imaging in SII **imaging by old method**

FIG. 9, Resistivity Imaging Of The New 3D Parallel GILD EM Nonlinear Inversion Using Crosshole Data

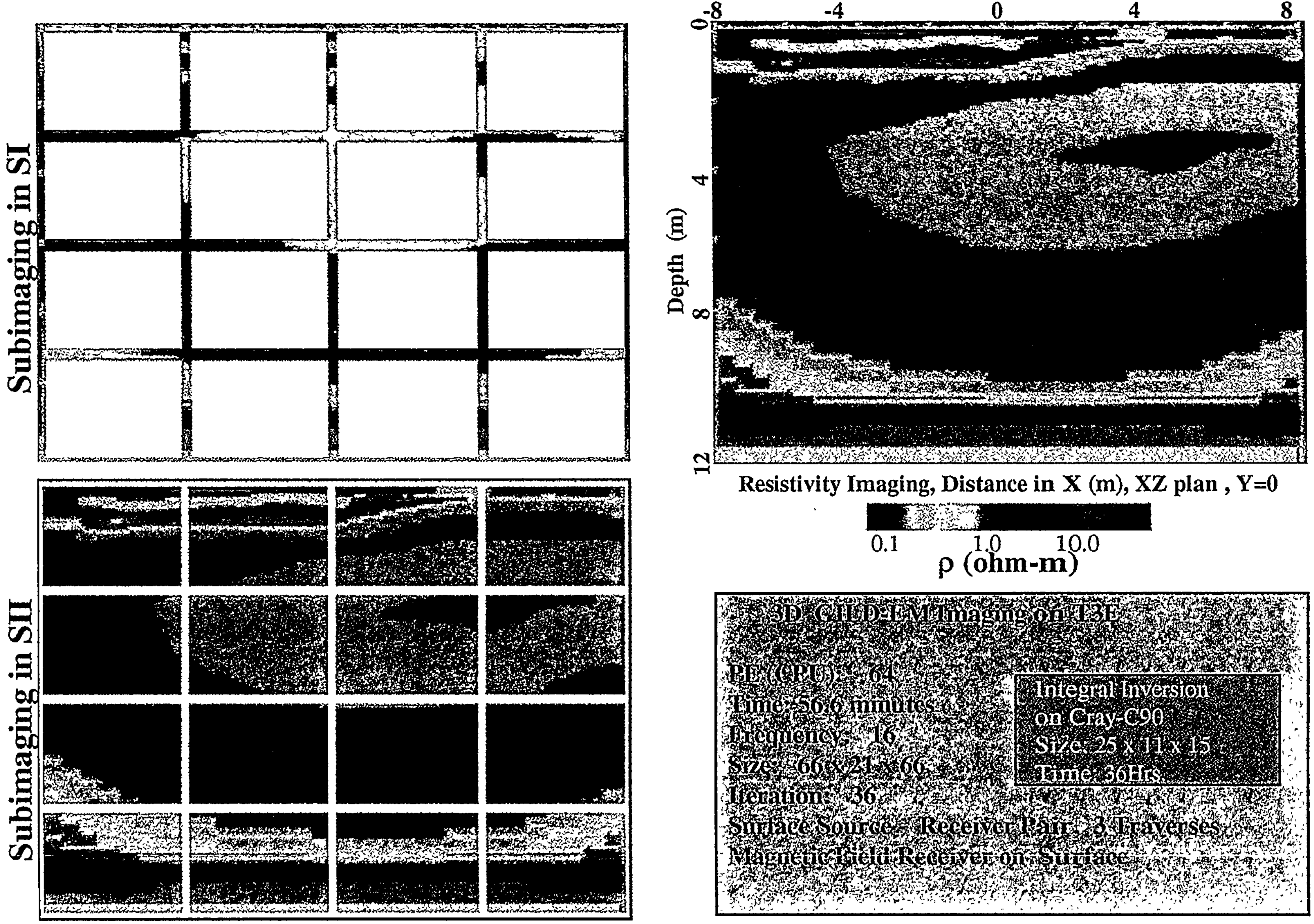

3D GILD-EM Imaging on T3E

PE (CPU): 64
Time: 56.6 minutes
Frequency: 16
Size: 66 x 21 x 66
Iteration: 36
Surface Source - Receiver Pair, 3 Traverses
Magnetic Field Receiver on Surface

Integral Inversion
on Cray-C90
Size: 25 x 11 x 15
Time: 36Hrs

Fig. 10 Parallel 3D GILD resistivity imaging for VETEM field data